



Design of an ethidium bromide control circuit supported by deep theoretical insight

Filip Vlahović^{a,1}, Miloš Ognjanović^{b,1}, Sladjana Djurdjić^c, Andrej Kukuruzar^c, Bratislav Antić^b, Biljana Dojčinović^a, Dalibor Stanković^{b,c,*}

^a University of Belgrade, Institute of Chemistry, Technology and Metallurgy - National Institute of the Republic of Serbia, Njegoševa 12, 11000 Belgrade, Serbia

^b University of Belgrade, VINČA Institute of Nuclear Sciences - National Institute of the Republic of Serbia, Mike Petrovića Alasa 12–14, 11000 Belgrade, Serbia

^c Faculty of Chemistry, University of Belgrade, Studentski trg 12–16, 11000 Belgrade, Serbia

ARTICLE INFO

Keywords:

Electrochemical advanced oxidation processes
Modified graphite anode
Submicromolar detection
Density functional theory
Fukui functions

ABSTRACT

We have set-up an electrochemical advanced oxidation process for ethidium bromide (**1**), based on the Eu-doped MnWO_4 (Eu:MnWO_4), obtained through a template-driven synthesis, along with developing a suitable monitoring method. Under galvanostatic conditions, Eu:MnWO_4 -coated graphite electrode serves as anode, applicable for removal of **1**. To go further and augment the catalytic method, we have applied a modified carbon paste electrode for the monitoring of **1** with the limit of detection (LOD) of 54 nM. Enhancement of the hydrogen evolution reaction is an indication of electrocatalytic properties of the material, whereby developed method emerges as a candidate for straightforward application in electrochemical advanced oxidation processes (EAOPs). We have enriched experimental data with theoretical insights, provided by Density Functional Theory (DFT), and proposed oxidation mechanism of **1**. Based on obtained results, we propose the new nanomaterial as a potent electrochemical modifier, suitable for catalytic treatment and process monitoring of the **1**-polluted waters.

1. Introduction

Ethidium bromide (**1**) is a dark red, non-volatile and water-soluble compound, widely used as a nucleic acid marker in electrophoresis, which is why it found an important application in various medical and pharmaceutical laboratories. This compound is predominantly available in the form of a diluted aqueous solution. Besides being non-radioactive, the main advantage of using this compound is its intense fluorescent response, which intensifies almost 20 times after binding (intercalating) to DNA [1]. Due to the fact that **1** specifically binds the information-carrying molecules, it is characterized by strong mutagenicity, carcinogenicity and teratogenicity depending on the organism and the circumstances of exposure [2]. Working with this material requires special protocols for handling and disposal. Methods for its removal and minimization of its release into watercourses and ecosystems, as well as the existence of rapid methods for its quantification and monitoring, are of crucial importance for the preservation of a healthy environment.

Up until now, several methods have been proposed for the efficient

degradation and removal of **1** from wastewater [3–9], while, to the best of our knowledge, electrochemical methods for its quantification, that can be found in the current literature, are limited to two papers [10,11]. Carbajo and co-workers proposed a method based on photocatalytic degradation, using hydrogen peroxide with bare titania (TiO_2) and iron-doped titania as catalysts [12]. A visible-light photocatalytic procedure, based on iron-modified titania, was proposed by Lavand and Malghe, where a remarkably efficient and catalyst-stable degradation of **1** was achieved [13]. Another similar photocatalytic degradation of **1**, utilizing TiO_2 , was proposed by Adan et al. [14]. In the scope of Fenton-like nanocatalyst-based reaction, Xie and co-workers also proposed a degradation pathway of **1** [15]. Two studies, based on boron-doped diamond (BDD) electrode anodic degradation of **1**, were provided by Zhang and co-workers with 80.2% [16] and complete removal efficiency [4]. Magnetic attapulgite- Fe_3O_4 nanocomposites, in the presence of hydrogen peroxide, showed 80% removal efficiency [17]. In the studies of Li et al. and Chang et al., two different absorption procedures were proposed for the removal of **1**, based on rectorite and palygorskite as working materials [7,9].

* Corresponding author at: Faculty of Chemistry, University of Belgrade, Studentski trg 12-16, 11000 Belgrade, Serbia.

E-mail address: dalibors@chem.bg.ac.rs (D. Stanković).

¹ these authors equally contributed to this work.

Although the determination and monitoring of **1** is very important, studies addressing this problem remain absent from the literature. Oliveira and Nascimento investigated the oxidation mechanism and possible determination of **1** using the glassy carbon electrode [10]. Two studies were reported by Matsumoto et al., where different approaches were taken aiming to immobilize DNA molecules at the electrode surface, in order to develop DNA biosensors for **1** detection [18,19].

Synthesis of nanostructured materials with unique properties, different from those of bulk materials, stands as an important field since newly-fabricated metallic, organic, inorganic and hybrid nanomaterials have an irreplaceable role in medicine, industry and technology [20]. The advantage of manganese tungstate compared to basic WO_3 lies in the synergistic effect of both semiconductor components. Manganese tungstate (MnWO_4) possesses a monoclinic wolframite-type structure with $[\text{WO}_6]/[\text{MnO}_6]$ clusters in distorted octahedra. In this material, the conduction band is formed by 5d orbitals of tungsten and the valence band (VB) mainly consists of hybridized O 2p with Mn 3d orbitals to dissipate the VB mainly in favor of photo-induced holes according to oxidation reactions. In addition, the bandgap of MnWO_4 (–2.80 eV) is more suitable for efficient visible light harvesting, and the positive position of VB may be beneficial for the generation of oxidative radicals [21–23]. Nanostructured MnWO_4 materials and their modifications exhibit unique electrical, electrochemical and photocatalytic behavior, which is well documented in literature [24–28]. Based on the aforementioned properties, these materials have already found application in EAOP removal of various organic pollutants in water. Doping can considerably augment existing and add new characteristics to the original materials, thus extending, the application possibilities [27,29,30].

Rare earth elements possess partially-filled 4f and completely occupied 5d orbitals, which intensifies surface light absorption and further separates resulting electron-hole pairs. For this reason, europium-doped materials show distinctive properties, suitable for application in different research fields, such as electrocatalysis, photocatalysis, photoelectrocatalysis, energy storage, etc, and thus remains in the scientific focus [31–33].

In the present work, the properties of a known MnWO_4 nanomaterial were altered and rationally tuned by introducing europium to the bulk material. This newly-fabricated nanomaterial was used for dual electrochemical application: development of an analytical method for the monitoring of the **1** concentration and an electrochemical procedure for successful removal of the pollutant from hospital wastewaters. The material itself was synthesized using a template-based procedure and characterized by morphological and electrochemical methods. We have

enriched our experimental work with theoretical insights, provided by Density Functional Theory (DFT) [34]. DFT represents an indispensable modeling toolbox, capable of investigating, explaining and most importantly predicting physico-chemical properties of both organic and inorganic molecules. DFT-based reactivity descriptors, such as Fukui functions [35–38], were widely used to predict the most probable reactive sites without actual calculations of the corresponding potential energy surface [39–42]. In this regard, within the DFT framework, we have calculated the condensed form of local Fukui functions and utilized this descriptor to theoretically determine the most reactive center(s) of **1**. Based on obtained theoretical insights, we have further proposed the oxidation mechanism of examined analyte.

This study suggests a remarkable application benefits of the same nanomaterial for both concentration monitoring and degradation of **1** in a real-time wastewater sample. The proposed research idea is summarized in Scheme 1.

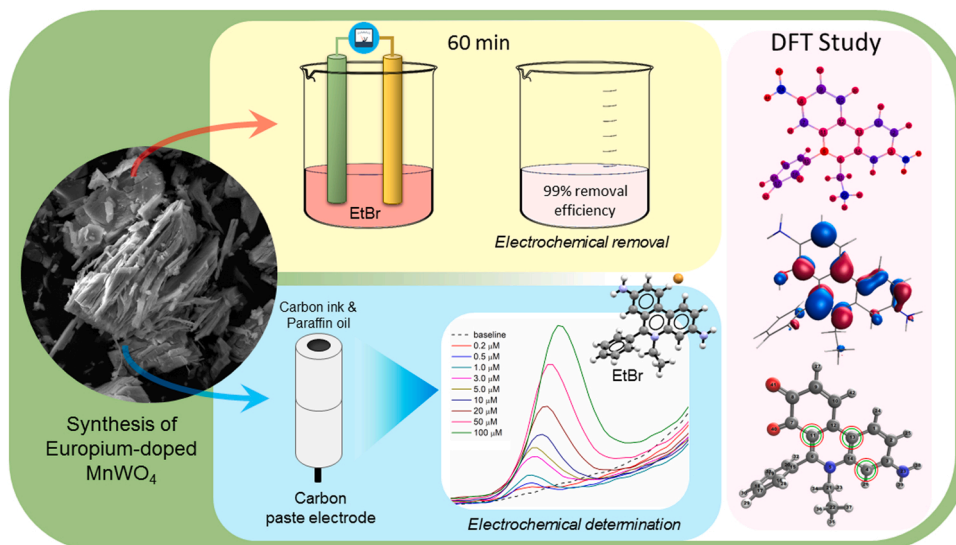
2. Experimental

2.1. Chemicals

All chemicals used in this study were supplied by Sigma Aldrich. Chemicals were of analytical grade and used as received. For solution preparation, double-distilled water was used.

2.2. Apparatuses

Degradation experiments were performed in undivided cells, containing 30 mL of 20 ppm **1** solution, equipped with unmodified or modified carbon rod electrodes. The carbon electrodes were 5 mm in diameter and 10 mm in length. The active surface area of the working part of the electrodes was 177 mm². During all experiments, the solutions were stirred to ensure homogeneity. The experiments were carried out under galvanostatic conditions with an adjustable DC power supply PS3010 (0–32 V DC, 0–10 A) E-HQ™. An UV-Visible spectrophotometer (Evolution 200 Series, Thermo Fisher Scientific, Bremen, Germany) was used for monitoring decolorization rates, at the maximum absorption wavelength $\lambda_{\text{max}} = 615$ nm. Cyclic voltammetry (CV) and square wave voltammetry (SWV) measurements, required for the development of the analytical procedure, were done using an electrochemical workstation (CHI 760B, CH Instruments, Austin, USA). The cell was equipped with a three-electrode system, comprising a working carbon-paste electrode (CPE) (modified or unmodified), a reference electrode (Ag/AgCl 3 M



Scheme 1. Schematic illustration of the work idea.

KCl), and a counter electrode (platinum wire). All measurements were performed at ambient temperature. The CPEs were produced by mixing glassy carbon powder (80%) and mineral oil (20%). For the modification procedure, the amount of introduced modifier was calculated as the percentage of graphite powder exclusively.

2.3. Synthesis of materials

The hollow carbon spheres, which were used as a template for further synthesis, were prepared as follows: 8 g of glucose was dissolved in 35 mL of water. The obtained solution was transferred into an autoclave and held at 160 °C for 9 h. The resulting black precipitate was washed three times with water, three times with ethanol, and then dried. The material thus obtained was used for further syntheses as prepared.

2.4. Template-based synthesis of Eu^{3+} -doped MnWO_4 catalyst

The Eu^{3+} -doped MnWO_4 catalyst (Eu:MnWO_4) was synthesized in a one-step hydrothermal procedure. Following the original preparation procedure for MnWO_4 [24], 2.5 mmol of $\text{Na}_2\text{WO}_4 \cdot 2 \text{H}_2\text{O}$ was dissolved in 10 mL of deionized water, and 5 mmol of $\text{Mn}(\text{NO}_3)_2$ was dissolved in 20 mL nitric acid solution (1 mol/L). Subsequently, the two solutions were mixed, whereby a white suspension was obtained. Stirring was applied for 2 h to ensure complete homogenization. A certain mass of $\text{Eu}(\text{NO}_3)_3$ (the molar ratio of $\text{Eu}(\text{NO}_3)_3$ to $\text{Na}_2\text{WO}_4 \cdot 2 \text{H}_2\text{O}$ was 7.5%) and 0.05 g polyvinylpyrrolidone (PVP, 40000) were added to the mixture, together with 0.03 g of hollow carbon spheres. For the sake of later material characteristics comparison, the same procedure was undertaken without the addition of $\text{Eu}(\text{NO}_3)_3$. The pH value of the mixture was adjusted to 4 using sodium hydroxide solution, and it was stirred for another hour. The obtained precursor suspension was transferred to a 100 mL autoclave and kept at 160 °C for 12 h in an oven. After the resulting pale-yellow Eu:MnWO_4 precipitate was cooled down to room temperature, it was washed several times with absolute ethanol and deionized water respectively, and finally dried at 60 °C for 10 h in an air flow. The same procedure was repeated for the MnWO_4 sample.

2.5. Characterization of materials

The crystal structure of prepared samples was determined using X-ray powder-diffraction (XRD) data measured on dried powders in a high-resolution SmartLab® diffractometer (Rigaku, Japan). The patterns were collected within the 10–70° 2 θ range at a scan rate of 1.5°/min under a voltage of 40 kV, a current of 30 mA and equipped with Cu K α radiation source ($\lambda = 1.5406 \text{ \AA}$).

Transmission Electron Microscopy (TEM) was used to determine the morphology and size of nanoparticles and check the samples' homogeneity. TEM analysis was performed on an FEI Talos F200X high-resolution transmission electron microscope (HR-TEM, Thermo Fisher Scientific, US) at an accelerating voltage of 200 kV, equipped with a CCD camera using the User Interface software package. An energy-dispersive X-ray spectroscopy (EDS) system attached to the TEM operating in the scanning transmission (STEM) mode was used for chemical analysis and element color mapping. High-angle annular dark-field (HAADF) images were captured in a nanoprobe with probes of below 1 nm size and a camera length of ~ 200 mm. A standard procedure prepared the samples for TEM examination. Solid powders were firstly dispersed into ethanol, placed dropwise on a carbon-coated copper grid and allowed to dry in the air for 24 h.

The morphology of MnWO_4 -based nanocatalysts were also examined using a field emission scanning electron microscope FE-SEM MIRA3 (Tescan, Czech Republic) operating at 20 keV. The samples were fixated on a holder with conductive tape, vacuum-dried, and spray-coated with gold using a Sputter coater. The size of catalyst particles was estimated by manual measurement using the public domain software ImageJ. Micrographs were recorded in different magnifications in the range

1000–50.000 \times .

3. Results and discussion

3.1. Selection of material – morphological and electrochemical properties

The rational design and synthesis of poly-functional catalysts represents the shortest path to improvement of existing industrial and technological concepts and methods. Selecting the appropriate material, based on its properties, plays supreme key role. Since the shape and size of the material components will strongly influence its general physico-chemical characteristics [30], it is important to take into account the desired final morphological aspects during each step of the synthetic process. Template synthesis of nanomaterials has emerged as a cutting-edge technology in the field of particle fabrication. Template-based methods are less sensitive to preparation conditions, they are easy to operate and implement, and most importantly, they ensure a direct control over the resulting material's structure, morphology, and particle size (through the initial size and structure of the template material) [43]. Encouraged by all these facts, we started the research by synthesizing template-based Eu:MnWO_4 nanoparticles, and further investigated the capability of this highly effective material in electrocatalysis. MnWO_4 showed excellent electrocatalytic properties, with a direct band gap of 2.56 eV, which is an explicit indication that this material is able to adsorb light of higher wavelength, and thus cover the major portion of the solar spectrum. Structural features of this material make it suitable for doping with other metals, which in turn can tune the initial band gap and ensure better photoelectrochemical efficiency [44]. The europium(III) ion possess the electronegativity of 1.2 and the standard electrode potential of – 1.991 V [45]. Based on these values, this material can act as a carrier suppressor, reducing carrier concentrations in the initial material. Due to the larger ionic radius of Eu^{3+} (1.07 Å) versus that of Mn^{2+} (0.89 Å), by doping of MnWO_4 with Eu^{3+} enhanced ionic conductivity with suitable lattice distortion can be achieved. Europium can be found as a doping agent in various functionalized nanomaterials [45,46]. Starting compounds were mixed in the stoichiometric ratio in order to obtain Eu:MnWO_4 with nominal composition $\text{Mn}_{0.95}\text{Eu}_{0.05}\text{WO}_4$ (with vacancies-denoted). The content of Eu, Mn and W in Eu:MnWO_4 was determined by inductively coupled plasma with optical emission spectroscopy (ICP-OES) (Thermo Fisher Scientific, iCAP some Duo ICP, Cambridge, UK: all details given in [Supplementary material](#)). Based on the elemental analysis, the chemical formulas of the samples were calculated and a small deviation in composition was determined. Namely, instead of 7.5% of Europium, a value of 5% was determined relative to all cations in the formula unit. Europium doping (or partial aliovalent cation substitution) of Mn^{2+} in host MnWO_4 influence a deviation from stoichiometry by forming cation vacancies, which further results in cation deficiency at manganese sites (Wyckoff position, 2 f) in wolframite structure (space group P2/c). Doping/substitution of Mn^{2+} by 3 + ions can significantly change magnetic properties of initial MnWO_4 and produce local distortions [47, 48]. Consequently, doping studied here influences electrical properties and redox reactions in the use of Eu:MnWO_4 as an electrocatalyst.

Crystal structure of the MnWO_4 as well as Eu:MnWO_4 was examined by X-ray diffraction technique (XRD), and the obtained XRD patterns are shown in [Fig. 1A](#). Reflection pattern of the crystalline phase correspond to the wolframite structure type (JCPDS No:72–0478). However, contamination of some other phases was noticed. By inspecting the crystallography database, a second phase, hydrated oxide of manganese tungsten ($\text{Mn}_4\text{W}_6\text{O}_{21}(\text{OH})_2 \cdot 4 \text{H}_2\text{O}$) was identified (JCPDS No:47–140) [49] in the MnWO_4 XRD pattern. Reflections belonging to this phase are denoted with \star . The XRD pattern of Eu:MnWO_4 match well with standard monoclinic MnWO_4 crystal system data and can be ascribed to the P2/c space-group symmetry (JCPDS No:72–0478). Only a small unidentified crystalline phase (marked with \diamond) was noticed.

The morphology and particle size of the samples were analyzed using

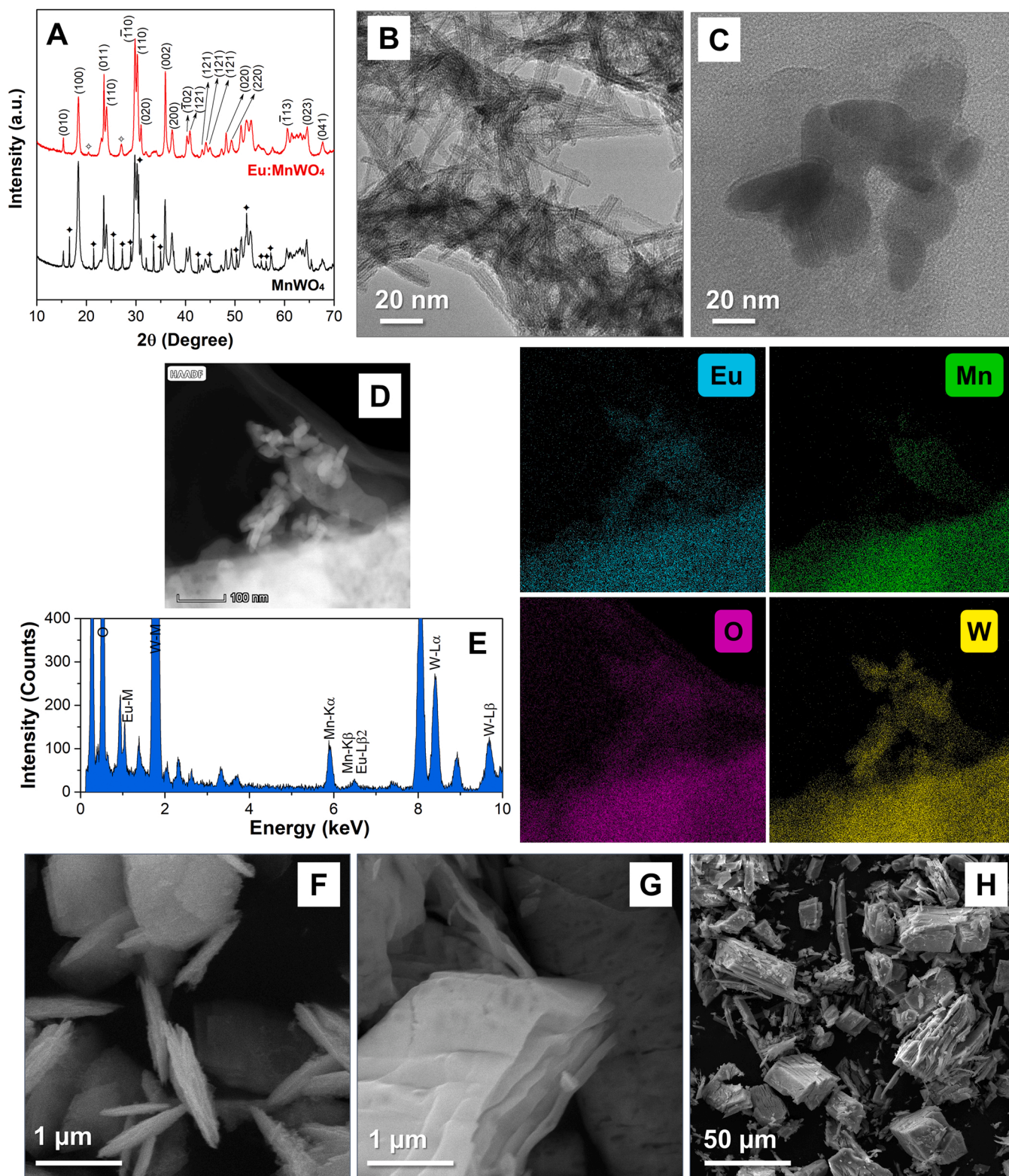


Fig. 1. (A) XRD diffraction patterns of MnWO₄ and Eu:MnWO₄ catalysts; (B) TEM micrograph of MnWO₄; (C) TEM micrograph of Eu:MnWO₄; (D) TEM-EDS analysis of Eu:MnWO₄. High resolution HAADF micrograph of the selected area with corresponding EDS elemental mapping of Eu, Mn, O and W; E) EDS spectrum; (F) FE-SEM micrograph of MnWO₄ and (G-H) Eu:MnWO₄ in different magnifications.

the transition electron microscopy (TEM). TEM micrographs of MnWO₄ and Eu:MnWO₄ are shown in Figures 1B and 1C, respectively. It can be seen that the particles of MnWO₄ are shaped rod-like with an estimated length of 60–80 nm and a width of about 5 nm. In the Eu:MnWO₄ sample, particles with different morphologies indicate a partial

substitution of Mn²⁺ by Eu³⁺, which influenced the crystallite growth. Nanorods, having a mean length of ~40 nm and width of ~15 nm, together with elongated pseudo-spherical particles with a mean diameter of about 20 nm, are the dominant components of Eu:MnWO₄. EDS elemental analysis of the selected area of the HAADF micrograph

showed that elements Eu, Mn, W and O were approximately uniformly distributed throughout the particles (Fig. 1D), indicating incorporation of europium into crystal lattice of the host MnWO_4 , rather than a mixture of particles with different chemical composition (1D-E). Elemental composition of Eu:MnWO_4 was also determined by ICP-OES, which can be considered as a more precise technique than the quantitative analysis of the EDS data. The morphology of the sample aggregates was also inspected by FE-SEM. Fig. 1F shows the formation of MnWO_4 as thin oval rectangles, close to disc-like shape, with an average diameter of about 1.2 μm . Thin sheets of material are stacked on top of each other, creating nanoforms with an average thickness of about 100 nm. On the other hand, Eu:MnWO_4 aggregates have a stacked rectangular cuboid shape, with slightly thicker layers of materials (~130 nm), which can be observed from Fig. 1G-H. Small particle diameters, observed experimentally, are a clear indication of a large number of atoms densely packed in the surface area, with compromised translational symmetry caused by the alteration of the initial coordination environment of the metal(s). Aliovalent cation substitution ($\text{Eu}^{3+} \rightarrow \text{Mn}^{2+}$) induces a non-stoichiometry in the sample and possibly a change in the oxidation state of the manganese ion.

For the investigation of the electrochemical properties of the material, we carried out CV measurements of $\text{Fe}^{2+/3+}$ redox couple in 0.1 M KCl, at the scan rate of 50 mV/s. Fig. 2A-B shows the presence of the modifier significantly improves the electrochemical characteristics of the bare CPE, by increasing the oxidation current and, at the same time, reducing the difference between the oxidation and reduction peaks (ΔE). For the detection of organic molecules, that are easily adsorbed onto the electrode surface, CPEs have huge advantages over other types of electrodes, primarily due to the possibility of (mechanical) surface renewal. On the other hand, due to the inhomogeneity of their surface, CPEs often show larger potential differences for the $\text{Fe}^{2+/3+}$ redox pair. The reduction of this value is a clear attestation that the electrochemical characteristics of the modified electrode have been boosted relative to the bare electrode – primarily the electron transfer process and acceleration of diffusion at the electrode/solution interface. The influence of the scan rate on the electrochemical performances of all working CPEs was measured and presented in Supplementary material, Fig. S1. Electrochemical impedance spectroscopy (EIS) was used in order to scrutinize the interfacial properties of the materials, as a key tool in determining charge transfer resistance, conductivity, electron transfer and diffusion characteristics at the electrode/solution interface. The EIS study was conducted in the frequency range from 0.01 Hz to 10^5 Hz with all prepared electrodes. A summary of obtained results is presented in the Fig. 2C. The equivalent circuit is provided as inset of Fig. 2C. The spectra are composed from two parts: first a semicircle part for the high frequency range, and a second linear part at low frequencies. The obtained R_{ct} values were in the following order: $\text{CPE} + 2\% \text{ Eu:MnWO}_4 < \text{CPE} + 5\% \text{ Eu:MnWO}_4 < \text{CPE} + 10\% \text{ Eu:MnWO}_4 < \text{CPE} + 7\% \text{ Eu:MnWO}_4 < \text{CPE} + 2\% \text{ MnWO}_4 < \text{CPE}$. The lowest R_{ct} value obtained for $\text{CPE} + 2\% \text{ Eu:MnWO}_4$ electrode, among other, indicates excellent surface properties: conductivity, wettability, fast charge transport, diffusion and electron transfer rate. All these facts suggest that the proposed hybrid nanocomposite can be a promising candidate for application in electrocatalysis.

Furthermore, the influence of the contribution (%) of Eu:MnWO_4 in the carbon paste on the hydrogen evolution reaction (HER) was evaluated. Due to a large number of experimental curves, for clarity, only the reduction part of the voltammograms (linear sweep voltammetry, LSV) of differently modified electrodes are shown in Fig. 3. The currents (I) were given as current densities (j), bearing in mind that the cross-sectional area of the working electrode is known (0.02544 cm^2), while the potentials were calculated relative to the reversible hydrogen electrode (RHE) using the equation: $E_{(\text{RHE})} = E_{(\text{Ag}/\text{AgCl})} + 0.197 + 0.059 \text{ pH}$. This standard potential represents the reversible potential of the reversible hydrogen electrode, and E vs. RHE can be conveniently denoted as overpotential (η). The highest activity for HER is achieved for the material where the reaction takes place at the smallest overpotential, for a certain value of current density (j). The HER kinetic parameters overpotential (η at 1 mA/cm^2) and Tafel slopes show a reduction in catalytic efficiency with increasing percentage of material in the CPE. The electrode modified with 5% of Eu:MnWO_4 had the best catalytic performance at pH 6, while at pH 9, the electrode with 2% of the material showed the best catalytic activity.

In the second phase we have carried out spectroelectrochemical measurements, in order to investigate the possibility to utilize our modifier for catalytic degradation of 1. The working printed carbon electrode (from the three-electrode system DRP C110) was modified with 5 microliters of 1 mg/mL modifier suspension in dimethyl sulfoxide (DMSO). After the electrode was dried, it was utilized for the electrochemical degradation, and the degradation rate of 1 was simultaneously monitored spectrophotometrically at different potentials over a period of 15 min. The resulting changes in the spectrum of 1, during degradation, are presented in Fig. 4A-E, while the dependence of the released current as a function of time is given in Fig. 4F. Fig. 4 shows that no degradation of analyte occurs at potentials below 1 V. With the increase of the potential to 1.5 V, the first results are obtained, which indicates that this potential can be used for the degradation process. It is important to notice that at this point, the degradation rate is very low. In contrast, increasing the potential to 2 V and further to 2.5 V, leads to both an increase in current and most importantly to faster degradation of the analyte. The most stable and continuous value of the current was obtained at a potential of 2.5 V, associated with the corresponding increase in the degradation rate of 1. For this reason, the potential of 2.5 V is considered as the minimum potential required to ensure the continuous and efficient degradation of the analyte.

The lowest R_{ct} value obtained for $\text{CPE} + 2\% \text{ Eu:MnWO}_4$ electrode, among other, indicates excellent surface properties: conductivity, wettability, fast charge transport, diffusion and electron transfer rate. All these facts suggest that the proposed hybrid nanocomposite can be a promising candidate for application in electrocatalysis.

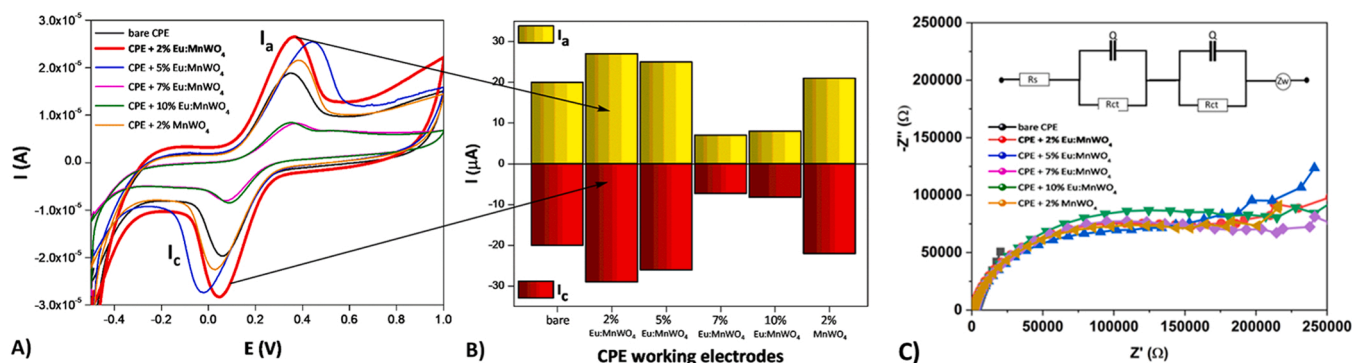


Fig. 2. A) Cyclic voltammetric response of the bare and modified CPEs with different percentage of modifiers (Eu:MnWO_4 and MnWO_4) in 0.1 M KCl containing $\text{Fe}^{2+/3+}$ redox couple; scan rate of 50 mV/s. B) Current intensities of anodic (I_a) and cathodic peak (I_c) over different CPE working electrodes at scan rate of 50 mV/s plotted as bar graph. C) EIS spectra for CPE working electrodes for the $\text{Fe}^{2+/3+}$ redox probe in 0.1 M KCl. Inset figure presents equivalent circuit.

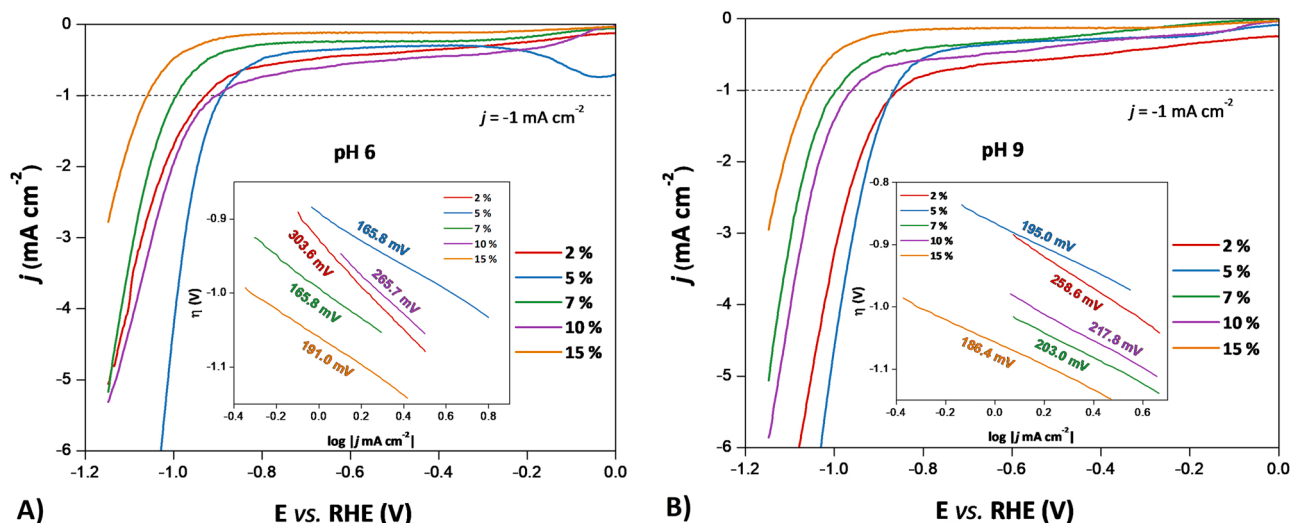


Fig. 3. Reduction part of CVs of differently modified electrodes in BRBS at (A) pH 6 and (B) pH 9. Corresponding Tafel plots are given as Figure insets.

4. Development of the analytical procedure for 1 detection

The first step in this part of the experimental study was the appraisal of our modifier for application in the determination and concentration monitoring of **1**. To investigate the influence of the amount of the modifier in the CPE, on the oxidation of **1**, square wave voltammetry (SWV) measurements were derived. The results are provided in Fig. 5 and show that the presence of the modifier significantly improves electrochemical characteristics of the CPE electrode, by increasing the intensity of the peak current (Fig. 5A). In addition, the modifier significantly stabilizes the electrochemical signal and reduces the residual current. The influence of the amount of modifier during the preparation of carbon paste was tested in the range from 2% to 10%. Obtained data show that the most stable peaks, with highest intensity of oxidation current, were obtained with the electrode containing 2% of modifier (Fig. 5B), and thus this concentration was selected for the development of the **1** detection method. From this point on, we will refer to CPE modified with 2% of Eu:MnWO₄ nanomaterial as the optimized electrode.

Further, we carried out cyclic voltammetry measurements in Britton-Robinson buffer solution (BRBS), at various pH (3–12), in order to find the proper parameters for development of the most sensitive and selective analytical method, with widest working linear range. These initial measurements hold double importance for the evolution of the method. Firstly, we can gather valuable information about catalytic properties, specificity of the electrode interface toward the selected analyte, reaction kinetics, as well as some insight into diffusion of the electroactive species and possible adsorption onto the electrode surface. Secondly, optimal pH determination will minimize the consumption of required chemicals, contributing to the “greening” of the method. Fig. 6A represents electrochemical behavior of the optimized electrode, at various pHs of BRBS containing 0.1 mM of **1**. The best electrochemical oxidation peak of **1**, by taking into account the peak shape and the peak current (based on background current subtraction), was achieved at pH 6. At pH values higher than 10, there is a high increase in the residual current (Fig. 6A), which strongly influence the resulting limit of detection (LOD) and limit of quantification (LOQ). In addition, starting from pH 7 (Fig. 6B) and going to more basic media, a linear change in the oxidation peak potential can be observed. This linearity can be expressed using the following equation: $E(V) = 1.1410 - 0.0587 \text{ pH}$, with Pearson's coefficient (r) of -0.982 . The obtained slope value is in ideal agreement with the theoretical slope of 0.059, typical for the processes where an equal number of protons and electrons is involved, which further indicates that we can hypothesize that the dominant peak

in this pH range originates from the formation of quinone derivatives. The reduction peak, observed in the reverse scan, is assigned to the reduction of the oxidized form of **1**, probably to the hydroquinone/quinone redox system [10]. However, detailed mechanism of action is proposed below.

4.1. Effect of the CV scan rate on the electrochemical oxidation response of 1

CV plots quantitatively assess the electrochemical kinetics, by varying the scan rate. In this regard, we have investigated the nature of the interface reaction by providing a CV profiling of the 0.1 mM of **1**, at pH 6 of BRBS, in the scan rate range from 5 to 200 mV/s. It is important to mention that after each scan, the electrode surface was renewed. Cyclic voltametric measurements showed redox behavior of **1** at the optimized electrode (oxidation at 0.73 V and reduction at -0.003 V) and a continuous increase in current with increasing of the scan rate (Fig. 7A). CV measurements were carried out in triplicate ($n = 3$). The dependence of the current intensity (I) on the square root of the scan rate ($v^{1/2}$) is shown in Fig. 7B. It can be concluded that the oxidation and reduction current peak of **1** linearly increases versus square root of the scan rate (Fig. 7B). These trends indicate a diffusion-controlled redox processes of **1**. However, in order to confirm these hypotheses, logarithm of current intensity ($\log I$) of redox peaks of **1** as a function of logarithm of scan rate ($\log v$) were plotted (Fig. 7C – oxidation peak, and 7D – reduction peak). From $\log I$ vs. $\log v$ dependence, a slope of 0.52 for oxidation peak (Fig. 7C) is very close to theoretical value of 0.5 and suggests diffusion-controlled process responsible for the oxidation of **1** at surface of optimized electrode. On the other hand, observing the slope of 0.94 for reduction peak (Fig. 7D) and taking into account the theoretical value of 1.00, reduction of **1** can be assigned to the adsorption-controlled process with slight contribution of diffusion.

4.2. Optimization of the detection method

Choosing the apposite detection method, characterized by the highest possible value of the oxidation current, is the final step in the optimization process of developed procedure. In this regard, we have investigated the electrochemical oxidation response of **1**, using SWV and differential pulse voltammetry (DPV). Comparison of the SWV/DPV obtained results, for the oxidation of 50 μM of **1** in BRBS at pH 6 is presented in Fig. 8A. Led by the almost two times higher current intensity, obtained with SWV, this method became the method of choice, and thus we proceeded to optimization of the corresponding parameters,

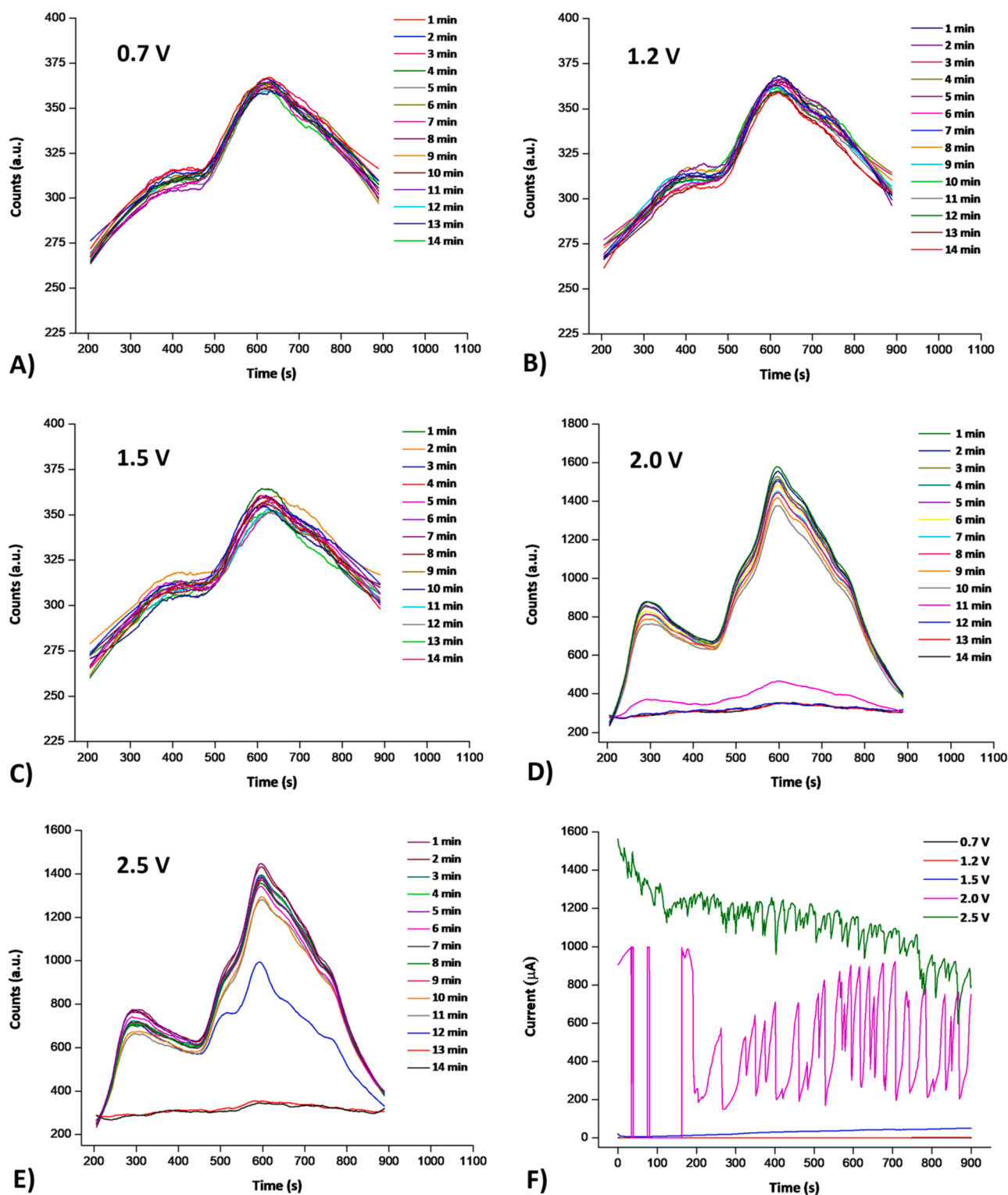


Fig. 4. Spectroelectrochemical spectra of **1** at different applied voltages: A) 0.7 V; B) 1.2 V; C) 1.5 V; D) 2.0 V; E) 2.5 V. F) Released current changes over the time at different applied voltages.

in optimal conditions (solution and working electrode). Differences in current intensity are visible in the variation of the following parameters: pulse step, pulse amplitude and pulse frequency (Fig. 8B-D, respectively). It is worthy to highlight that during the optimization of one parameter, the other two were kept at a constant value. Finally, selected parameters for the method were: pulse step of 14 mV, pulse amplitude of 40 mV and frequency of 50 Hz. During the selection of these parameters,

beside the current intensity, we also took into account the shape and width of the peak. Encouraged by the results (in optimal conditions), we are now able to carry out the calibration measurements, interference studies, reproducibility and repeatability investigation, and as a crown of this research, test the accuracy and precision through a real-world sample analysis.

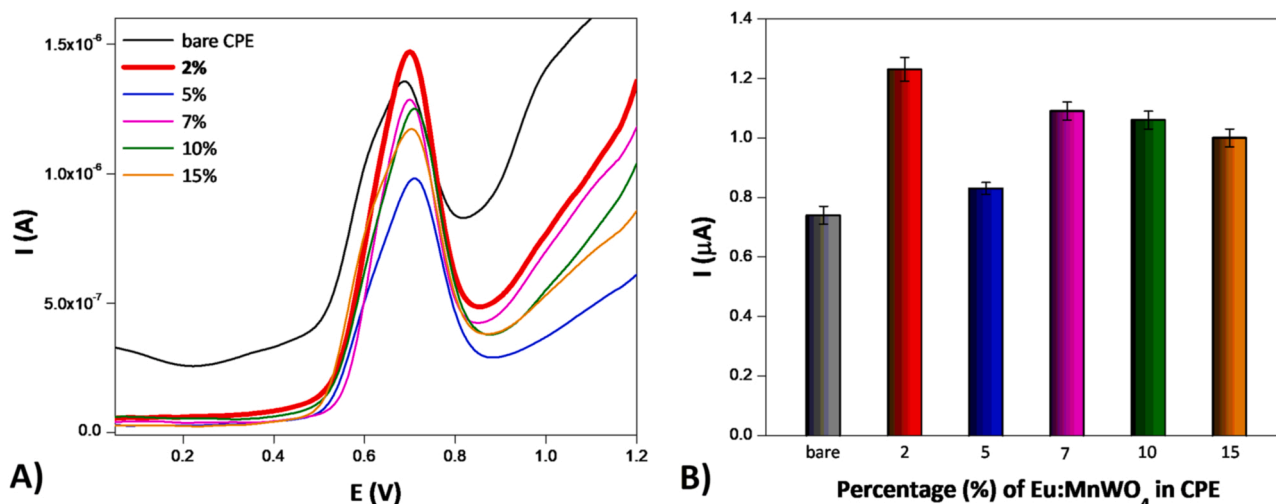


Fig. 5. A) SW voltammograms of bare and CPEs modified with different percentage (2%, 5%, 7%, 10% and 15%) of Eu:MnWO₄ recorder in BRBS pH 6 containing 10 μM of 1. SWV parameters: frequency of 50 Hz, pulse amplitude of 40 mV and pulse step of 14 mV. B) Individual current intensity of 1 oxidation peak for different CPE working electrodes plotted as bar diagram.

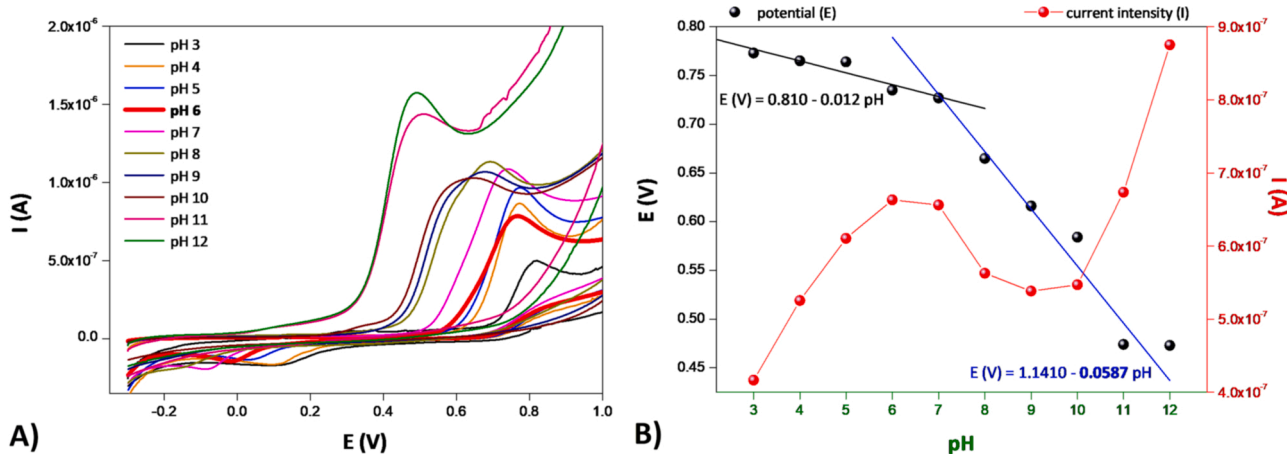


Fig. 6. A) Effect of different pHs of BRBS at electrochemical oxidation of 1 (0.1 mM) using optimized electrode; scan rate of 100 mV/s. B) Plot of current intensity (I) and peak potential (E) vs. pH.

4.3. Analytical characteristics – SWV for 1 different concentration over developed sensor

Based on obtained experimental results, SWV technique was chosen over DPV, and used for contemporaneous detection of 1, due to its superior resolution and current intensity. The concurrent measurement of 1 was accomplished by an optimized electrode in BRBS pH 6, under previously optimized parameters. Fig. 9A shows the respective SW voltammograms, where the optimized electrode recorded oxidation of 1 in a wide concentration range from 0.2 to 80 μM. The calibration measurements were performed in triplicate. Fig. 9B shows the plot of current intensity (I) vs. logarithm of 1 concentration (log C), where two linear segments are clearly observed. The corresponding error bars at Fig. 9B represent standard deviation between measurements (n = 3). First segment of linearity, in the concentration range from 0.2 to 7 μM, can be expressed using the following equations: $I(\mu A) = 0.90 \log C(\mu M) + 0.99$ ($r = 0.992$). Second linearity area is described by equation: $I(\mu A) = 3.44 \log C(\mu M) - 0.99$ ($r = 0.994$), and corresponds to the concentration range from 7 to 80 μM. LOD and LOQ were calculated from the first linear segment as $LOD = 3S_{y/x}/\text{slope}$ and $LOQ = 10S_{y/x}/\text{slope}$, and were estimated to be 0.054 μM and 0.171 μM, respectively. Repeatability and reproducibility of the method were investigated in the BRBS

of pH 6, containing 5 μM of 1 and using the following approach (under optimized SWV parameters): for repeatability - 10 measurements of this solution during one day (intraday study) using the optimized electrode; for reproducibility - 5 independently prepared optimized electrodes during five days (interday study). Relative standard deviations (RSDs) for all these measurements were lower than 3.7%, indicating excellent accuracy and precision of the method, with the wide operable linear range.

4.4. Optimization of the degradation procedure of 1, using the Eu: MnWO₄ coated graphite electrode

Activity of the anode material, catalytic reactions, as well as side reactions such as oxygen (hydrogen) evolution reactions, have different catalytic activity and kinetics in acidic, basic and neutral media, what greatly affects the final parameters of the developed method. For this reason, pH choice will play a crucial role in the degradation process. In this paper, the optimal pH (pH 6) was chosen based on testing the behavior of 1 at different pH values (see above), as well as HER/OER measurements, and further applied during the optimization of all important parameters, in order to achieve the best possible characteristics for the method. In this regard, the influence of the supporting

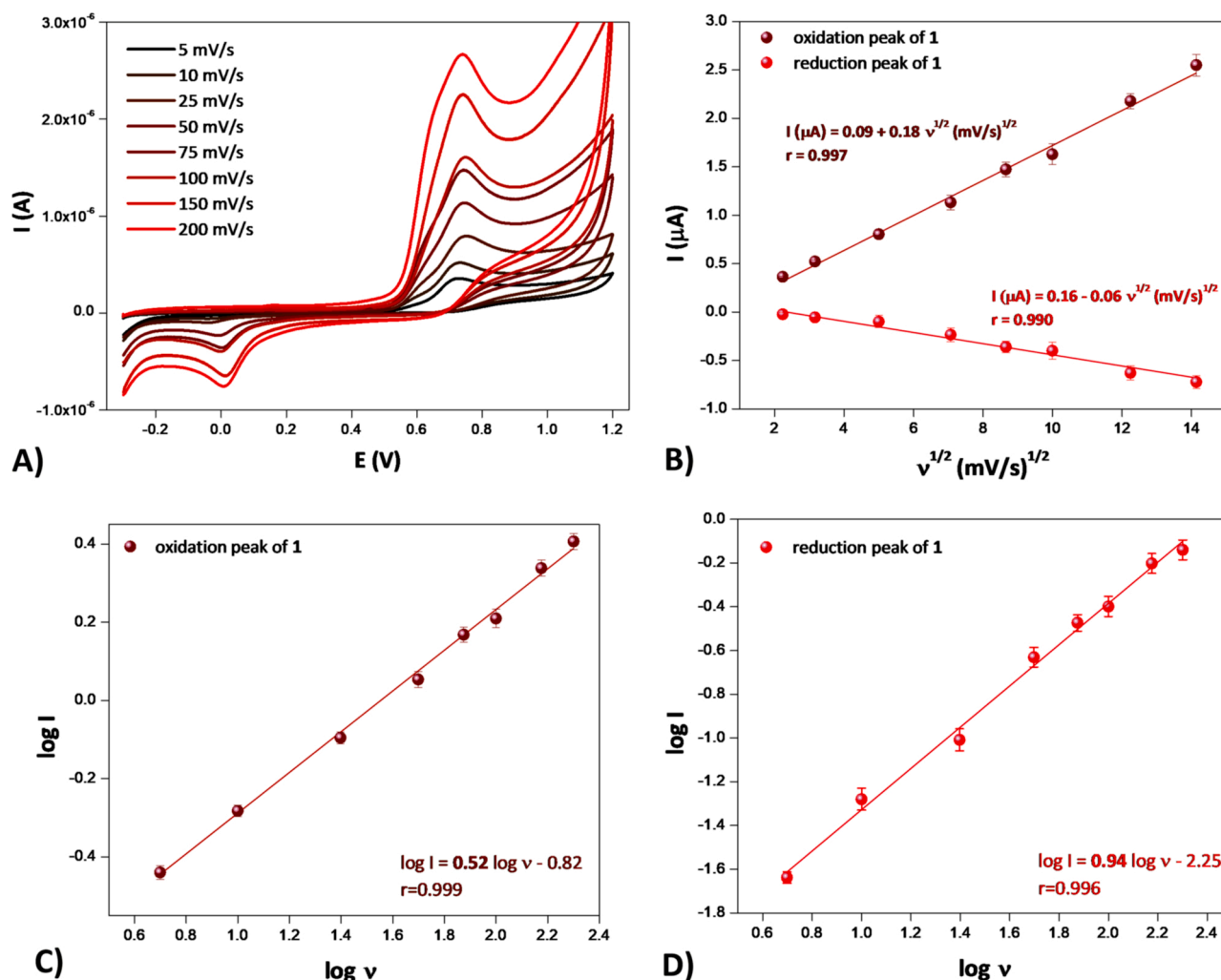


Fig. 7. A) CV voltammograms of 1 (0.1 mM) in BRBS pH 6 at various scan rates. B) Plot of dependence of the oxidation/reduction peak current (I) of 1 vs. square root of the scan rate ($v^{1/2}$). Error bars represent standard deviation between measurements ($n = 3$). C) $\log I$ vs. $\log v$ plot for the oxidation peak of 1 with corresponding error bars. D) $\log I$ vs. $\log v$ plot for the reduction peak of 1 with corresponding error bars.

electrolyte choice, its concentration, as well as the intensity of the applied current were examined in order to maximize the degree of energy utilization, and simultaneously maximize the degradation efficiency. To determine the optimal composition of the supporting electrolyte, sodium salts (sodium nitrate and sodium sulfate) were tested. These salts have an advantage important for all fields where electrolytic processes are taking place, because they can often be found in industrial applications as companions of wastewater and have excellent electrochemical characteristics (conductivity, inertness, and stable oxidation state). Data representing the effect of the supporting electrolyte, in the concentration of 0.1 M, toward degradation efficiency of the 1 (20 ppm), at the potential of 5 V are given in the Fig. 10A. The better degradation efficiency (higher degree rate) was obtained with the sodium sulfate supporting electrolyte. Around 50% better results indicate that this salt should be used for further development of the procedure. For additional optimization of the method, we have tested the influence of concentration of the chosen supporting electrolyte in the range from 0.01 to 0.10 M (at the potential of 5 V), on the degradation efficiency of 1. The results are shown in Fig. 10B. The optimal (minimum) concentration of the electrolyte, which hopefully also enables the highest rate of degradation, can significantly lower the cost of the method, and enhance the green character of the technique. As expected, with the increase of electrolyte concentration, the efficiency of 1 degradation increases, during 60 min of treatment. However, although

it would be expected for the degradation efficiency to have the highest values at maximum sodium sulfate concentrations, the best results were obtained in the solution containing 0.02 M of the electrolyte. The conductivity of the wastewater solution is very low, and by increasing electrolyte concentration, the mass transfer improves, which gives a huge impact to the overall reaction rate. Yet, if we take into account the speed and efficiency of proposed degradation method, we can conclude that the ion concentration during the degradation process increases significantly, and thus higher concentrations of the supporting electrolyte will suppress the reaction. This phenomenon can be also attributed to the larger number of possible side reactions on the electrodes (caused by the presence of a large number of ions) or the consumption of energy for the heating of the solution. By increasing the concentration above 0.02 M, the increase in efficiency becomes less noticeable, or leads to a decrease in the overall rate of degradation. The decrease in removal rate, above concentration of 0.02 M of the electrolyte, can be connected with the generation of fewer oxidant species at higher electrolyte concentrations, due to increased production of $S_2O_8^{2-}$, originating from the sulfate ions [50,51]. It should be noted that in all the probes using the selected concentrations, the removal of 1 was carried out up to nearly 100%. At the very end of the method optimization, the influence of the applied voltage (current density) on the degradation efficiency was examined (Fig. 10C). This parameter is of utmost importance for electrochemical degradation processes, and its determination is very

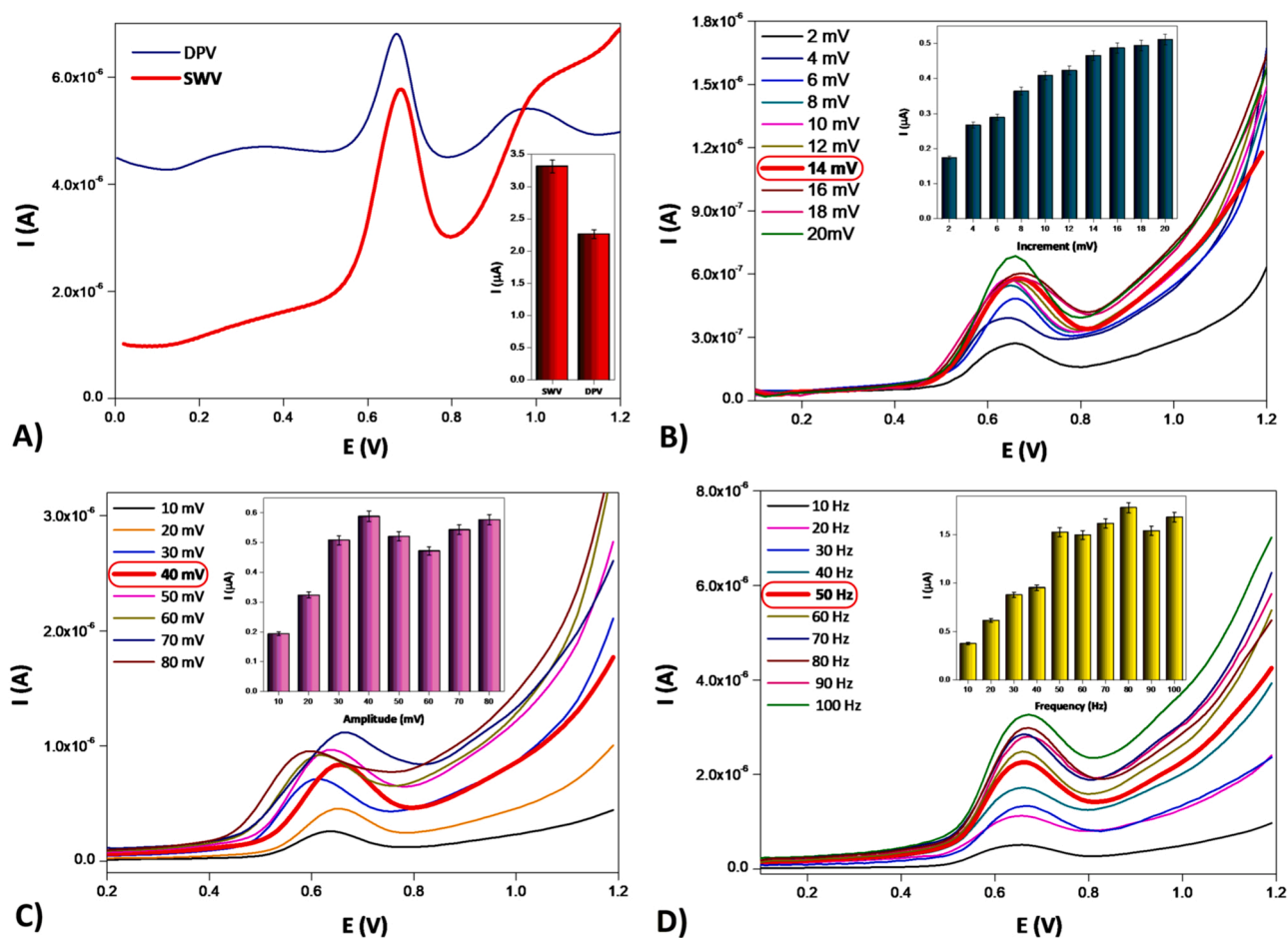


Fig. 8. A) Comparison of DPV and SWV methods for oxidation of 50 μM of **1** in BRBS at pH 6. SW voltametric profile of 50 μM of **1** in BRBS pH 6 recorded at different SWV parameters: B) pulse step, C) pulse amplitude and D) frequency.

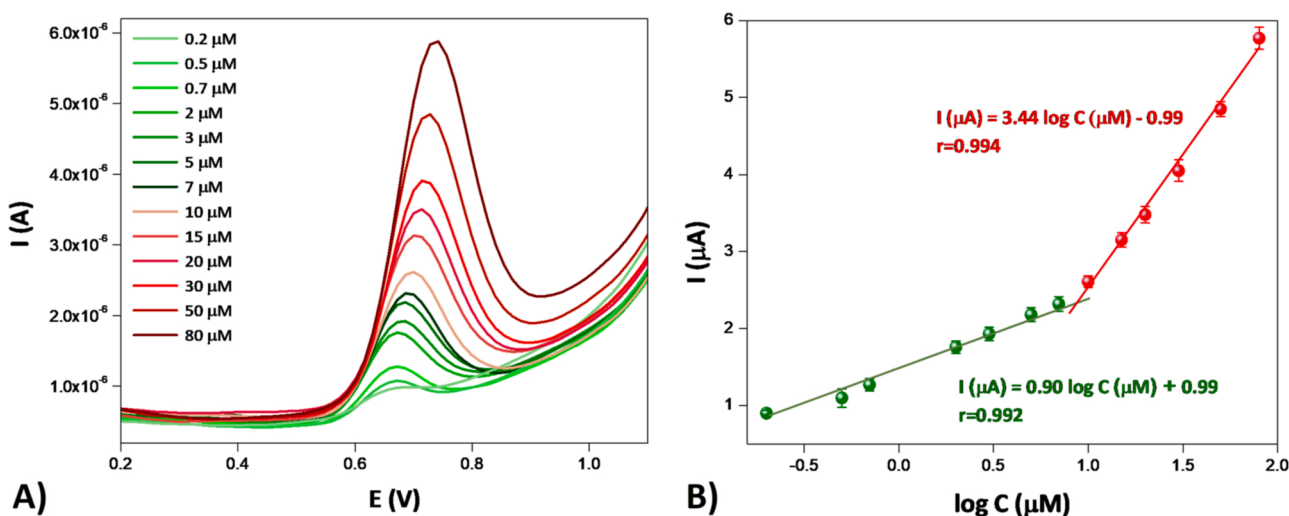


Fig. 9. A) SW records for the different concentrations of **1** in BRBS pH 6 on the optimized electrode. SWV parameters: pulse step of 14 mV, pulse amplitude of 40 mV and frequency of 50 Hz. B) Linear plot between current intensity (I) and logarithm of **1** concentration ($\log C$) with corresponding error bars ($n = 3$).

important, since the energy consumption should be as low as possible, with highest possible pollutant removal effect. In that sense, the influence of different applied working voltages on the **1** removal rate, in the range from 1.5 to 7.0 V, was tested. On the electrode surface of 177 mm², the obtained current densities for each of the applied voltages were as follows: 1.5 V \rightarrow 15 mA/cm²; 3 V \rightarrow 27 mA/cm²; 5 V \rightarrow

48 mA/cm²; and 7 V \rightarrow 65 mA/cm². The obtained results are summarized in Fig. 10C, which shows that the increase of the applied voltage leads to the increase in removal efficiency until 5 V (48 mA/cm²). The most noticeable effect of the applied voltage was obtained with the increase from 1.5 V to 3 V. This is in accordance with the spectroelectrochemical studies, where we proved that the minimum value of

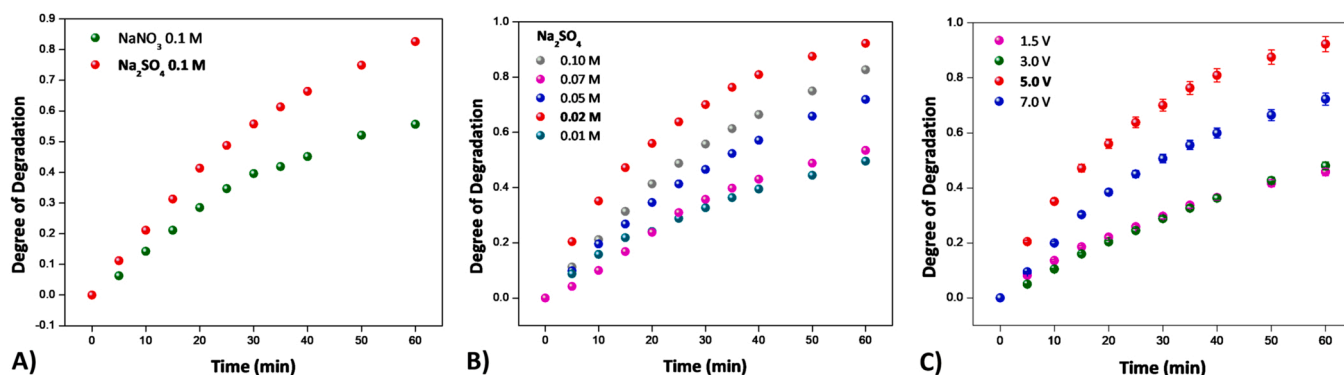


Fig. 10. A) Effect of the different supporting electrolytes for the removal of 20 ppm of **1**; applied potential of 5 V. B) Effect of different concentrations of Na_2SO_4 for the removal of 20 ppm of **1** at potential of 5 V. C) Effect of the applied voltage (current densities) for the degradation of 20 ppm of **1**.

applied voltage for continuous degradation was 2.5 V. The increase of the working voltage to the value of 5 V increases generation of reactive species and promotes removal. The decrease in the removal rate with the increase of the voltage/current above the value of 5 V, is probably due to the side reactions, where this value increases the generation rate of reactive species (moreover, bubbles produced at this point can have an inhibitory effect on the interfacial reaction between the electrode surface and reaction (testing) solution). Based on this experiment, the applied voltage of 5 V was determined to be optimal for the electrochemical degradation process. The final parameters of the degradation method can be summarized as following: optimal pH 6 of the solution, sodium sulfate as the supporting electrolyte at a concentration of 0.02 M, and a set voltage of 5 V, which corresponds to a current density of 48 mA/cm^2 .

4.5. Quantum chemical calculations, reaction mechanism and theoretical modeling of the experiment

Based on the nature of electrochemical process, in which removal/addition of electrons is involved, we aim to shed a light upon the experimental response of **1** through theoretical determination of its complex electronic structure. Our goal is also to investigate and understand the changes in the ground-state electronic structure, caused by conducted experiments. The quantum chemical calculations have been carried out with Orca [52] electronic structure program suite (Program Version 5.0.2), by using DFT approach (detailed computational information can be found in the [Supplementary material](#)). Hybrid B3LYP [33] functional, coupled with def2-TZVP basis set, have been chosen for calculation of structural and electronic properties of all chemical species of interest. Atomic charges, based on Mulliken [53,54] analysis, were utilized to analyse electronic character of molecular regions, as well as the reactivity of different sites within a molecule.

Obtained results, based on Mulliken charges ([Fig. 11A](#), [Table S1](#)),

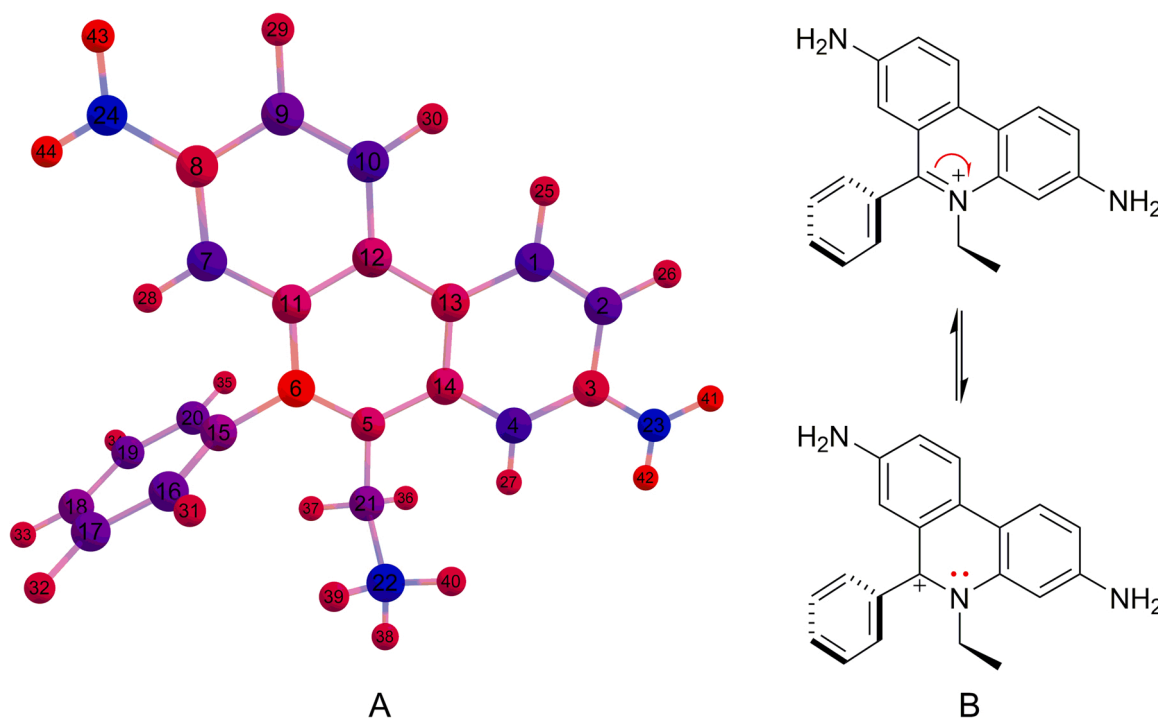


Fig. 11. A) Color representation of Mulliken charges, calculated for **1**, on B3LYP-D3BJ level of theory (calculated numeric values are given in the [Supplementary material](#), [Table S1](#)). Red color represents positively charged atoms, whereas blue represents negative centers of the molecule. B) Resonance hybrid-structure, responsible for electron-deficient character of carbon atom 6.

show a large electron density delocalization, with positive charge dominantly preserved in the central aromatic ring of the phenanthridinium core (including endocyclic nitrogen atom 5), and major negative charge shared between exocyclic amino groups, located on positions 3 and 8. Amino group located on position 8 emerges as a stronger base and contains more negative charge, than the group located on position 3, which can be explained by the fact that only amino group located on the position 3 has a possibility to delocalize its electron density to the quaternary nitrogen atom 5 through resonance [55,56]. This phenomenon directly influences and explains the differences in pKa

values of $pK_{a1} = 2.0$ and $pK_{a2} = 0.8$ respectively, as well as much weaker, if any, reactivity of later, electronically inactivated, group towards weak electrophiles [55–57]. It is important to highlight that although the calculations determined both exocyclic amino groups as negatively charged, these groups are considerably less basic than the amino group of aniline ($pK_a = 4.6$), which suggests an overall electron deficit character, when compared to other amines. Our observations are in a good qualitative agreement with the theoretical study provided by Hobza et al. [58], yet contrary to works in which a positive π -charge is proposed for all nitrogen atoms of **1** [56,59]. Reason for the mentioned

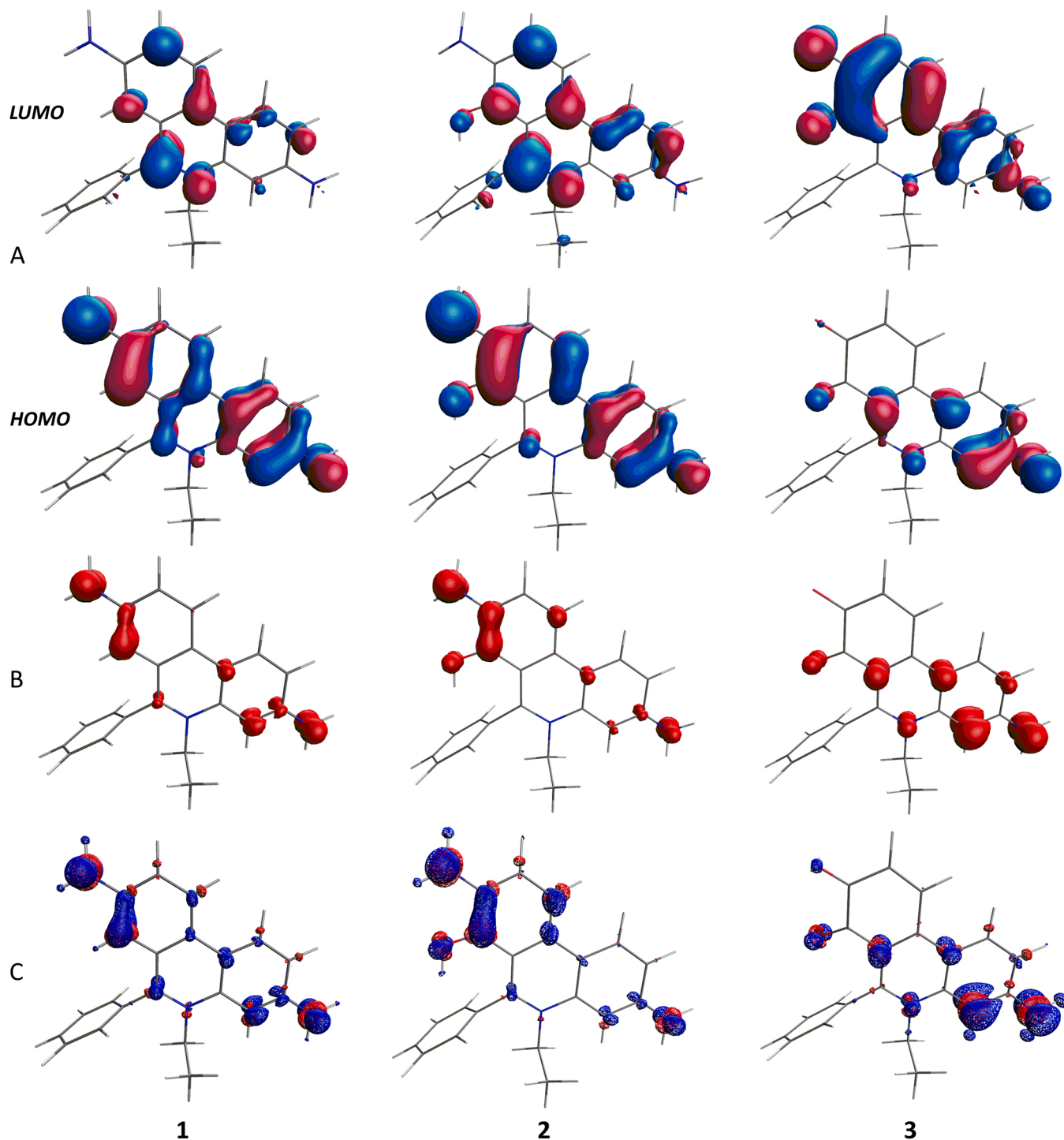


Fig. 12. A) HOMO and LUMO orbitals B) spin-density, generated after one-electron oxidation process C) isosurface plot of the Fukui function for a nucleophilic attack; for **1**, first oxidation product **2**, and final oxidation product **3**; calculations carried out on B3LYP-D3BJ level of theory.

differences lies within the experimental/theoretical conditions, including method accuracy, presence of the counter ion, solvation effects, or the accuracy of crystal structure used for the calculation of the partial charges. Due to the nature of our electrochemical experiments, we calculated the values of a fully-relaxed molecular structure (with solvation effects included and no counter ion present), in contrast to the calculations provided by extraction and utilization of crystal structure parameters [56].

Our Mulliken charge analysis (Table S1.) assigned carbon atom 6 as the most positive atomic center, which is already confirmed theoretically [59], as well as experimentally, since this center was demonstrated to be the reduction site of **1**, by a chemical reaction with sodium borohydride [60]. This can be explained by a simple charge transfer resonance structure, shown in Fig. 11B, which can be expected as one of the dominant structures in the resonance equilibrium of **1**, due to the electron withdrawing character of nitrogen 5.

In order to gain further insight into quantum chemical characteristics of **1** (and all main oxidation products), we continue our examination by

inspection of Highest Occupied Molecular Orbital (HOMO) and Lowest Unoccupied Molecular Orbital (LUMO). These orbitals are of utmost importance for present research since the shape and positioning (distribution) of these orbitals are directly correlated with electrochemical events. According to the molecular orbital theory, HOMO orbital energy represents the electron donating ability of one molecule when interacting with others. On the contrary, LUMO orbital energy denotes the electron accepting ability. In this regard, we can expect the removal of an electron to take place within the HOMO orbital (whereby a spin-density is generated in that region), whereas the addition of an electron or an electron pair from a donor, should have their main impact on the LUMO orbital. Although various valuable information can be extracted from frontier orbitals, it cannot tell us much about the reactivity of different sites within a specific molecule, and for this reason we further augment the observation by calculation of condensed local Fukui functions, as explained in the Supplementary material. It is important to consider these aspects together, in order to draw the final conclusion that will lead to the oxidation mechanism of **1**.

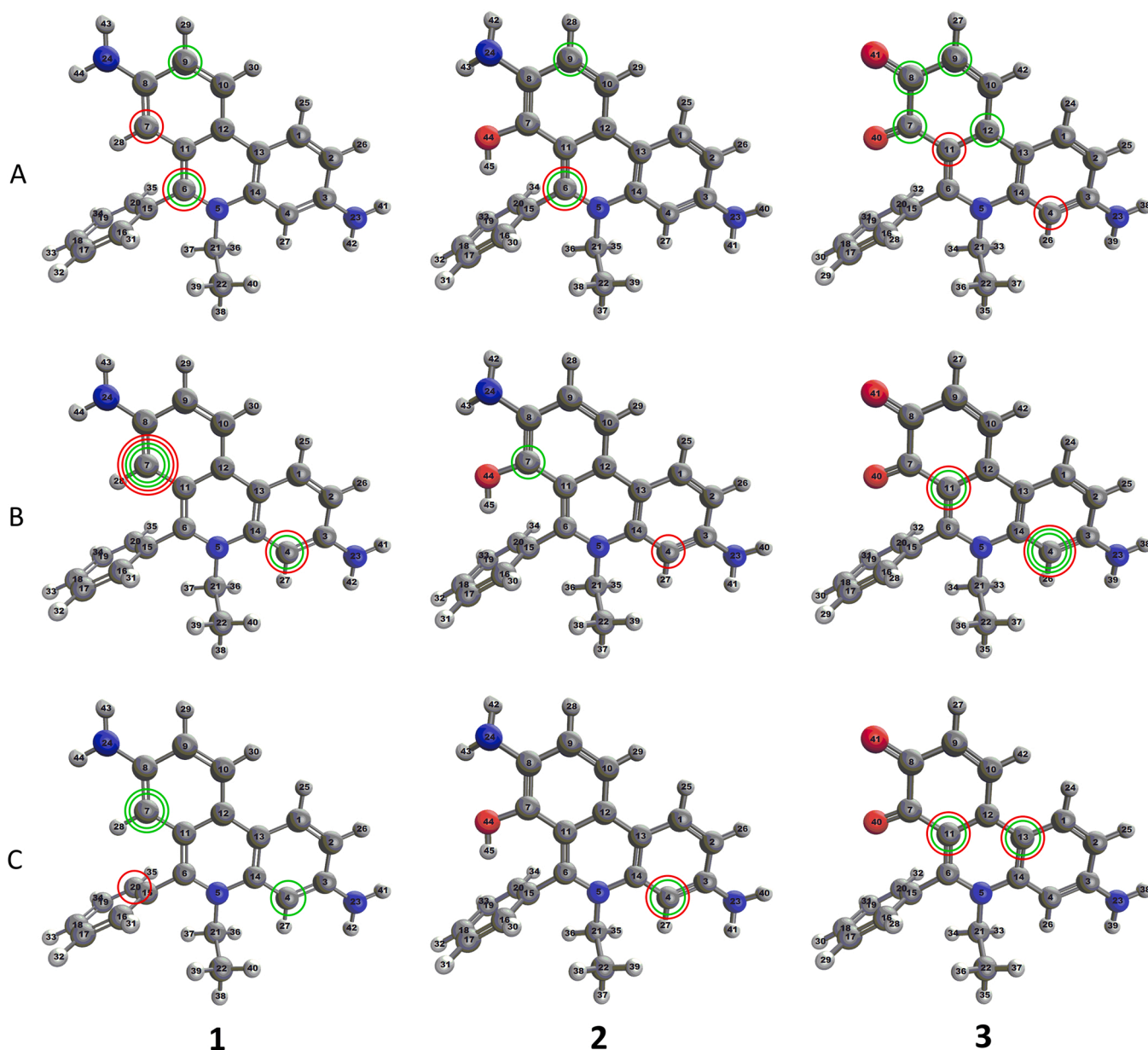


Fig. 13. Fukui functions- based reactive centers, susceptible to nucleophilic (green cycles) and radical (red cycles) attack A) Neutral species B) one-electron oxidized species C) two-electron oxidized species of **1**, first oxidation product **2**, and final oxidation product **3**; calculations carried out on B3LYP-D3BJ level of theory.

As we already mentioned, the first oxidation peak occurring in CV measurements of **1** (Fig. S5), corresponds to a single-electron oxidation event. The shape and distribution of HOMO orbital of **1** (Fig. 12. 1A) clearly reveals larger investment of the amino group located on the position 8, and thus, we can expect the electron density, formed by the removal of one electron (and formation of 1^+), to be dominantly concentrated in this region. The spin-density isosurface plot, shown in Fig. 12. 1B, proves our initial hypothesis, and with this information in mind we continue further analysis aiming to establish a correlation with the Fukui functions. Three Fukui functions represent reactivity towards electrophiles, nucleophiles and radicals, yet we will consider and discuss only the last two. Our analyte(s) will be electrochemically oxidized (transformed into cationic adducts), and as such prone to the nucleophilic attack of the water molecules present in the solution. Here, we shall not neglect the formation of hydroxyl radicals, on the electrode surface, that will also act as a reactive species. Although we have calculated the Fukui functions even for the neutral molecules (Fig. 13. 1A 2A 3 A), we consider this molecular form as inert, and their oxidized (charged) adducts as reactive moieties (Fig. 13. 1B-C 2B-C 3B-C). Calculations clearly show that after one-electron oxidation process takes place, **1** becomes susceptible to both nucleophilic and radical attack on the position 7, whereas a hydroxylated adduct **2** is formed. Based on obtained results, we declare the carbon atom 7 as the most reactive atomic center, of mono-oxidized **1**. Interestingly, this position retains its reactivity toward nucleophiles even after the second one-electron oxidation, but loses its initial susceptibility to radical attacks (Fig. 13. 1C). This phenomenon can be explained by general increase of the positive charge, together with the disappearance of the spin density,

caused by the removal of the final electron from the HOMO orbital. It is important to draw attention to a clear correlation between the spin-density and the attack topology/affinity of reactive species present in the matrix. In this regard, we also provide an isosurface plot of the Fukui function for a nucleophilic attack (Fig. 12. 1C). Our calculations also revealed the possibility for both nucleophilic and radical attack on analogous position 4, neighboring the second amino group (Fig. 13. 1B-C). Based on the numeric values, and the distribution of spin-density, we consider the resulting molecule **2a** as a side reaction product, yet we provided calculations for this and all corresponding chemical species involved in this alternative oxidation pathway (Fig. S2, Table S3).

Now that we have identified the first oxidation product **2**, we are able to continue our examination further in the direction of the final oxidation product. The shape and distribution of HOMO and LUMO orbitals of compound **2** did not change qualitatively, compared to the **1**, thus we expect the spin-density, generated by the one electron oxidation, to populate the same region as in the case of **1**. Isosurface plot of generated spin-density, as well as the plot of corresponding nucleophilic Fukui function (Fig. 12. 2B-C) shows that the chemical reaction, induced by electrochemical oxidation, should take place in the region of the amino group on position 8 and newly introduced hydroxyl group on position 7. Based on calculated numeric values (Table S2.), the reactivity of position 7 towards nucleophilic attack is retained (Fig. 13. 2B). Thus, we can expect further oxidation of already present functional groups, since the corresponding reaction would lead to the formation of the same product. After the second one-electron oxidation, position 4 of examined molecular species becomes susceptible to both nucleophilic and radical attack (Fig. 13. 2C), which would lead to the formation of an adduct

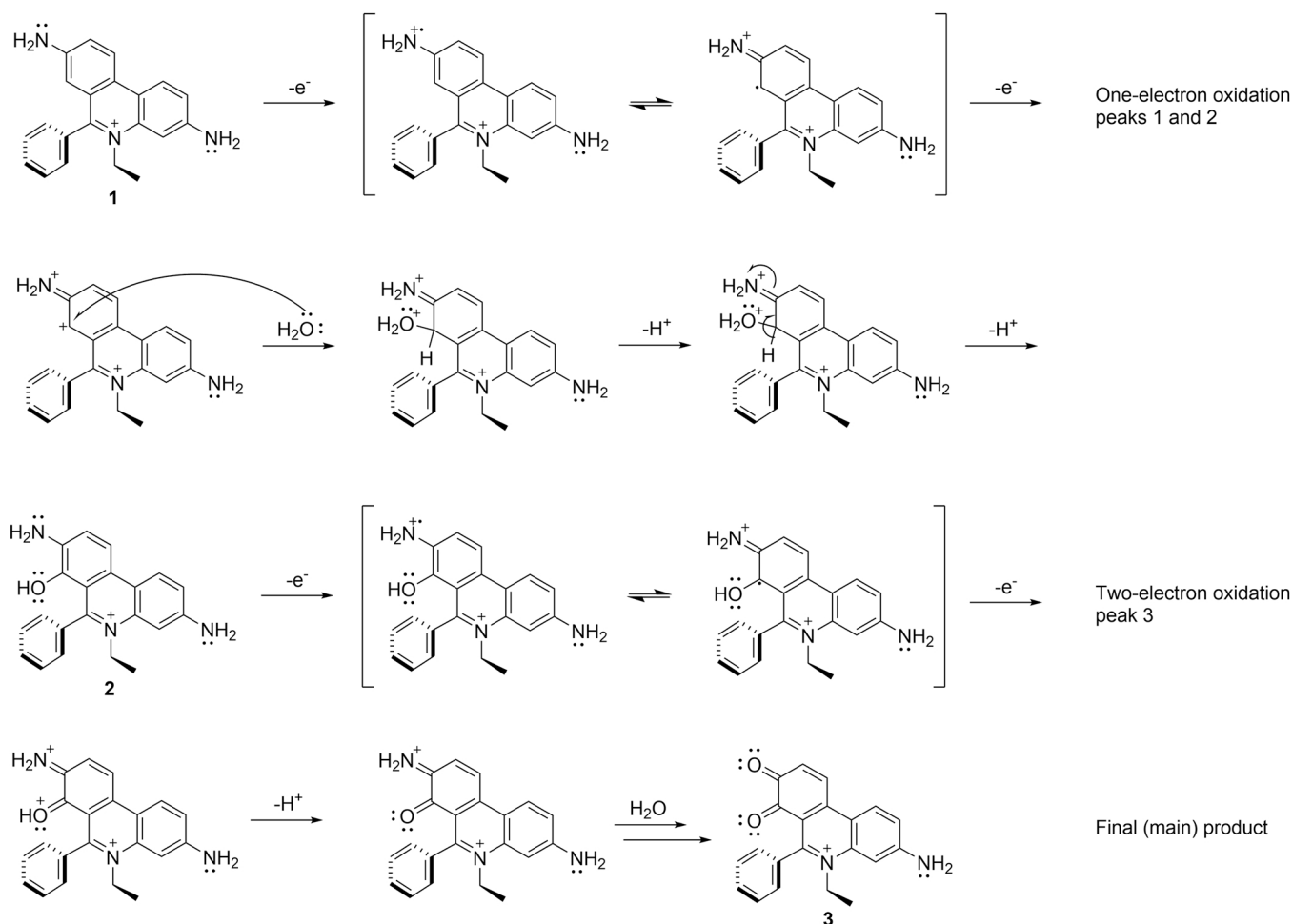


Fig. 14. Proposed oxidation mechanism of **1**, at working pH = 6, based on theoretical insights.

containing two hydroxyl groups, yet we consider the resulting product as a less probable side product.

Based on the theoretical investigation, we are now in position to assign, with more confidence, all experimentally obtained peaks, and propose a complete oxidation mechanism of **1** (Fig. 14). First two one-electron oxidation peaks are associated with the oxidation of amino group located on position 8. In the first oxidation step, one electron is removed from the HOMO orbital, whereby a radical cation is formed and further oxidized in the second (one electron) step to corresponding carbocation on position 7. Newly formed reactive center is subjected to direct nucleophilic attack by a water molecule, resulting in the formation of hydroxylated product **2**. Second oxidation peak, originating from a two-electron oxidation, corresponds to the oxidation of the same amino group, and successive formation of iminium cation, presented in the bottom-right part of the Fig. 14. Newly formed molecular species undergoes a well-known, water-promoted hydrolysis [61–63], resulting in the formation of final *ortho*-quinone derivative **3**. All potential side products can be observed in the Fig. S2, provided in the Supplementary material.

Calculation of the Fukui functions for the final product **3** (Table S4) led us to one important conclusion, related with oxidative degradation of **1**. Namely, in contrast to **1** and first oxidation-step product **2**, removal of the first electron from the HOMO orbital of product **3**, generates a spin-density (Fig. 13. 3B) with a considerable portion aggregated in the central aromatic ring of the phenanthridinium core (positions 11 and 13). Calculated values indicate that after one-electron oxidation, carbon atom 4 emerges as the most reactive center, yet a great probability for both nucleophilic and radical attack can be donated to carbon atom 11. Most importantly, the overall picture changes drastically after second one-electron oxidation, since the probability for a nucleophilic attack shifts to carbon centers 11 and 13. Considered together, obtained results lead us to conclude that after the final oxidation product **3** has been formed (together with potential side-products), the central aromatic ring of the phenanthridinium core becomes reactive and prone to the attack of active species present in the solution. In contrast to periphery aromatic rings, all these reactions would lead to the destabilization of aromatic core, breaking of chemical bonds and thus decomposition of the structure. In this regard we certainly believe that any further electrochemically induced change in the structure **3** will result in oxidative degradation.

Final part of our experimental research, urging for theoretical assistance, is the change of **1** behavior relative to the changes in pH of the working environment. This change is reflected through the change of UV/Vis spectra (Fig. S6) as well as changes observed in the obtained voltammograms (Fig. S5) on different pH. Most importantly, by taking a closer look at Figs. 6 and S5, three clusters can be observed; first in the range pH= 3–7, second at pH= 8–10, and the final one in the pH= 11–12. As we mentioned earlier, pKa values of **1** are pKa1 = 2.0 and pKa2 = 0.8 respectively, thus we can expect the protonation process to take place on the pH values lower than 2, and the first group which undergoes this process is the group on the position 8. Aiming to investigate the electronic structure and chemical behavior of the monoprotonated structure **1a** (Fig. S3), we have carried out a geometry optimization of this adduct. By keeping in mind previously mentioned pKa (4.6) and pKb= 9.30 [55] value of aniline, we can assume that the pKb value of **1** will be shifted by approximately the same level of magnitude as the pKa. In this regard, we can expect the deprotonation of **1** to take place at an approximate value of pH~8. As it can be seen from the experimental UV/vis (Fig. S6), a strong decrease of the first absorption band occurs at this exact pH. We believe that this pH represents the equilibrium point, in which half of the neutral **1** is being deprotonated, due to the increased basic character of the matrix. This assumption is confirmed by the pH-dependent voltammogram, shown in the Fig. S5, where a clear split of the initial peak into two, almost merged, peaks can be observed. This phenomenon indicates the presence of two nearly identical chemical species, differing only in the electron density.

The first group that will undergo the deprotonation process will be the amino group located at the position 3 (Fig. S3), leading to the formation of mono-deprotonated adduct **1b**, which we have also fully optimized. Based on the shape and the intensity of the peak(s), we can say that neutral **1** dominates over deprotonated adduct **1b** (Figure S6) until pH= 10 is reached, where **1b** becomes the most abundant molecular species.

As we already mentioned before, based on the molecular orbital theory, the energy gap ELUMO-EHOMO represents the energy needed for one electron to migrate from the HOMO and populate the LUMO. As a result, ELUMO-EHOMO correlates directly to the chemical stability of a molecule, with higher value showing more stability. In this regard, calculated ELUMO-EHOMO values for three molecular species (**1**, **1a** and **1b**) should reflect their stability and thus the energy required for the removal of an electron during the oxidation process. As it can be seen from the Table S8, the energy gap increases in order: **1b**<**1**<**1a**, which further explains the positions of oxidation peaks on measured voltammogram (Fig. S5), depending on the pH of the working environment.

To finalize our research, we have calculated corresponding Fukui functions for both **1a** and **1b** (Table S6 and S7). Conducted calculations suggest that protonation of **1** will be followed by a drastic change in the reactivity, and thus a change in the final reaction product. Namely, based on obtained Fukui functions, carbon atoms 4 and 13 become the most reactive centers of **1a** (Table S6, Fig. S4), after both one-electron and two-electron oxidation. This change in the reactivity would probably lead to formation of molecule **3a** (Fig. S2), which is the most probable side product generated in our initial experiment. Interestingly, after removal of the second electron benzene ring becomes susceptible to radical attack, which would result with the formation of phenols. For the double protonated structure, extreme acidic conditions must be achieved (mineral acid solutions), and since our working pH range is determined by BRBS buffer solution, we did not include this possibility in our theoretical investigation. Next step was the calculation of Fukui functions (Table S7, Figure S4) for the deprotonated adduct **1b**. Our calculations indicate pronounced reactivity of the carbon atom 4 even in the basic conditions, after both one-electron and two-electron oxidation. In this regard, we can again expect the side products from our initial experiment, at pH= 6 (Figure S2), to become the main products in basic conditions, and vice versa. Since this observation steps out of the scope of present research, and requires considerable amounts of both experimental and theoretical work, we will stop here, and hopefully provide further investigation in the future.

Finally, guided by our experiments and encouraged with theoretically collected insight, we proposed an oxidation mechanism of **1**, on optimal working pH= 6, through which it chemically changes to form **2** and finally product **3**. Our theoretical work opens a window to a whole new chemical landscape of **1** behavior, and sheds a light not only on obtained experimental results, but also on fundamental aspects of **1** complicated electronic structure. By defining the changes in the electronic structure, caused by the change of the working environment, we are able to understand the experiment, and hopefully in the future predict the result.

4.6. Application of the developed methods for the degradation of **1** and process monitoring

In order to investigate the possibility for practical application of the method, we have investigated efficiency of the degradation procedure in the pipe water, spiked with the 20 ppm of **1**, and most importantly, monitored the process with proposed analytical procedure. As a validation method UV/Vis measurements were carried out separately. Results are summarized in Fig. 15. The experiment confirmed that both methods can be successfully applied for the purpose they have been designed for. Efficiency of the degradation in a real sample was at the almost similar level as in distilled water, while monitoring with the proposed method was fully in accordance with the UV/Vis method.

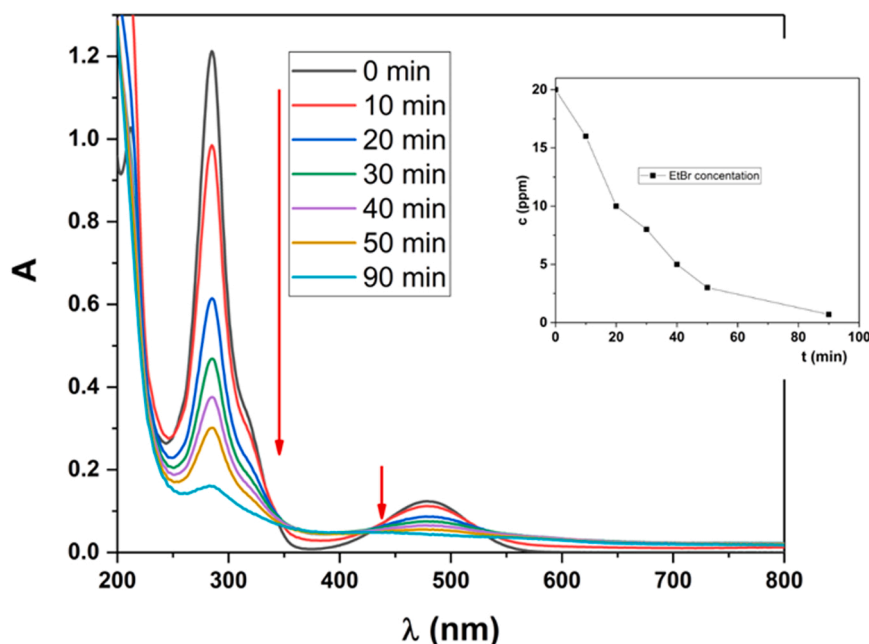


Fig. 15. Changes in the adsorption spectra of **1** during treatment of pipe water. Inset figure presents changes in **1** concentration during this process monitored with our developed method. Experiments were done under optimized methods parameters: applied voltage of 5 V, supporting electrolyte 0.02 M Na₂SO₄, and pH 6 of starting solution.

Additionally, under the given conditions, we examined changes in chemical oxygen demand (COD) and total carbon concentration (TOC), as well as degradation products monitored with high-performance liquid chromatography (HPLC). The corresponding chromatograms and the working procedures are given in Supplementary Material and Figure S7. The course of degradation under applied conditions leads to a significant decrease in the concentration of **1**. After every 15 min, the number of products obtained increases significantly, while the signal of **1** decreases about 37 times. These results confirm the successful degradation of **1** and the generation of a large number of different (small) molecules as a result of the treatment. An important parameter that determines the quality of a method is COD and TOC. After only one hour of treatment, the difference in the COD values of the starting solution and the treated solution was over 53% (76 mgO/L vs 36 mgO/L). At the same time the TOC values were: 33.6 mg/L before the treatment and 18.7 mg/L after the treatment. The decrease of 44.6% indicates excellent efficiency of the developed procedure.

5. Conclusions

In this study, a novel material Eu³⁺-doped MnWO₄ was successfully synthesized and utilized for dual electrochemical application - development of the procedure for effective degradation of ethidium bromide from wastewaters, and the development of an analytical tool for the monitoring of this process. The incorporation of the europium ions in the wolframite structure strongly influences its (spectro)electrochemical properties and morphological characteristics. By incorporating ~ 5% of Eu³⁺ into the crystal lattice of nanorods, the morphology of the particles changes to quasi-spherical and rod like with different length/width. Obtained materials serves as an excellent sensor for the **1** monitoring with the wide operating range, starting from submicromolar level of 0.2–80 μM. Calculated detection limit is 54 nM. Optimal (minimal) conditions for continuous degradation were found, through a spectroelectrochemical investigation, and further supported by the theoretically proposed possible degradation pathway. More than 50% of COD and more than 44% of TOC was decreased after one hour of treatment in optimal conditions, which included the voltage of 5 V, concentration of 0.02 M Na₂SO₄ supporting electrolyte and pH 6 of starting solution. This

work shows that selection of appropriate material plays the most important role, and that combination of nanotechnology, electrochemistry, theoretical and environmental chemistry can open a door for diverse applications of nanomaterials. The analytical procedure developed herein, based on functionalized carbon electrodes, can serve as a strong foundation for the development of disposable ethidium bromide sensors (together with a platform for its removal) and find its application in (medical) laboratory use and commercialization.

CRediT authorship contribution statement

Filip Vlahović: Data curation, Investigation, Methodology, Writing – original draft, Writing – review & editing. **Miloš Ognjanović:** Data curation, Investigation, Methodology, Writing – original draft, Writing – review & editing. **Sladjana Djurdjić:** Data curation, Investigation, Methodology. **Andrej Kukuruzar:** Data curation, Investigation. **Bratislav Antić:** Writing – original draft, Writing – review & editing. **Biljana Dojčnović:** Methodology, Writing – original draft, Writing – review & editing. **Dalibor Stanković:** Methodology, Writing – original draft, Writing – review & editing, Formal analysis, Resources, Supervision.

Declaration of Competing Interest

The authors declare that they have no known competing financial interests or personal relationships that could have appeared to influence the work reported in this paper.

Data availability

No data was used for the research described in the article.

Acknowledgement

This work was financially supported by the Ministry of Science, Technological Development and Innovation of Republic of Serbia, contract No: 451-03-47/2023-01/200168 and EUREKA project E!13303.

Appendix A. Supporting information

Supplementary data associated with this article can be found in the online version at [doi:10.1016/j.apcatb.2023.122819](https://doi.org/10.1016/j.apcatb.2023.122819).

References

- Supplementary data associated with this article can be found in the online version at [doi:10.1016/j.apcatb.2023.122819](https://doi.org/10.1016/j.apcatb.2023.122819).
- ## References
- [1] S. Thititananukij, R. Vejaratpimol, T. Pewnim, A.W. Fast, Ethidium bromide nuclear staining and fluorescence microscopy: an alternative method for triploidy detection in fish, *J. World Aquac. Soc.* 27 (1996) 213–217, <https://doi.org/10.1111/j.1749-7345.1996.tb00272.x>.
 - [2] V.L. Singer, T.E. Lawlor, S. Yue, Comparison of SYBR® Green I nucleic acid gel stain mutagenicity and ethidium bromide mutagenicity in the Salmonella/mammalian microsome reverse mutation assay (Ames test), *Mutat. Res. / Genet. Toxicol. Environ. Mutagen.* 439 (1999) 37–47, [https://doi.org/10.1016/S1383-5718\(98\)00172-7](https://doi.org/10.1016/S1383-5718(98)00172-7).
 - [3] E. Xie, L. Zheng, A. Ding, D. Zhang, Mechanisms and pathways of ethidium bromide Fenton-like degradation by reusable magnetic nanocatalysts, *Chemosphere* 262 (2021), 127852, <https://doi.org/10.1016/j.chemosphere.2020.127852>.
 - [4] C. Zhang, L. Liu, J. Wang, F. Rong, D. Fu, Electrochemical degradation of ethidium bromide using boron-doped diamond electrode, *Sep. Purif. Technol.* 107 (2013) 91–101, <https://doi.org/10.1016/j.seppur.2013.01.033>.
 - [5] M.N. Alnajrani, O.A. Alsager, Decomposition of DNA staining agent ethidium bromide by gamma irradiation: Conditions, kinetics, by-products, biological activity, and removal from wastewater, *J. Hazard. Mater.* 389 (2020), 122142, <https://doi.org/10.1016/j.jhazmat.2020.122142>.
 - [6] Z. Ge, T. Sun, J. Xing, X. Fan, Efficient removal of ethidium bromide from aqueous solution by using DNA-loaded Fe3O4 nanoparticles, *Environ. Sci. Pollut. Res.* 26 (2019) 2387–2396, <https://doi.org/10.1007/s11356-018-3747-7>.
 - [7] P.-H. Chang, B. Sarkar, Mechanistic insights into ethidium bromide removal by polyglycolite from contaminated water, *J. Environ. Manag.* 278 (2021), 111586, <https://doi.org/10.1016/j.jenvman.2020.111586>.
 - [8] A. Fakhri, Assessment of Ethidium bromide and Ethidium monoazide bromide removal from aqueous matrices by adsorption on cupric oxide nanoparticles, *Ecotoxicol. Environ. Saf.* 104 (2014) 386–392, <https://doi.org/10.1016/j.ecoenv.2013.12.017>.
 - [9] Z. Li, P.-H. Chang, W.-T. Jiang, Y. Liu, Enhanced removal of ethidium bromide (EtBr) from aqueous solution using rectorite, *J. Hazard. Mater.* 384 (2020), 121254, <https://doi.org/10.1016/j.jhazmat.2019.121254>.
 - [10] S.C.B. Oliveira, V.B. Nascimento, Electrochemical Oxidation Mechanism of Ethidium Bromide at a Glassy Carbon Electrode, *Electroanalysis* 25 (2013) 2117–2123, <https://doi.org/10.1002/elan.201300222>.
 - [11] J. He, B. Fugetsu, S. Tanaka, Electrochemical detection of ethidium bromide by using pure single-walled carbon nanotube sheet as the electrode, *J. Electroanal. Chem.* 638 (2010) 46–50, <https://doi.org/10.1016/j.jelechem.2009.10.022>.
 - [12] J. Carbajo, C. Adán, A. Rey, A. Martínez-Arias, A. Bahamonde, Optimization of H2O2 use during the photocatalytic degradation of ethidium bromide with TiO2 and iron-doped TiO2 catalysts, *Appl. Catal. B: Environ.* 102 (2011) 85–93, <https://doi.org/10.1016/j.apcatb.2010.11.028>.
 - [13] A.B. Lavand, Y.S. Malghe, Visible-light photocatalytic degradation of ethidium bromide using carbon- and iron-modified TiO2 photocatalyst, *J. Therm. Anal. Calor.* 123 (2016) 1163–1172, <https://doi.org/10.1007/s10973-015-5041-y>.
 - [14] C. Adán, A. Martínez-Arias, M. Fernández-García, A. Bahamonde, Photocatalytic degradation of ethidium bromide over titania in aqueous solutions, *Appl. Catal. B: Environ.* 76 (2007) 395–402, <https://doi.org/10.1016/j.apcatb.2007.06.013>.
 - [15] E. Xie, L. Zheng, A. Ding, D. Zhang, Mechanisms and pathways of ethidium bromide Fenton-like degradation by reusable magnetic nanocatalysts, *Chemosphere* 262 (2021), 127852, <https://doi.org/10.1016/j.chemosphere.2020.127852>.
 - [16] C. Zhang, L. Yang, F. Rong, D. Fu, Z. Gu, Boron-doped diamond anodic oxidation of ethidium bromide: Process optimization by response surface methodology, *Electrochim. Acta* 64 (2012) 100–109, <https://doi.org/10.1016/j.electacta.2011.12.122>.
 - [17] S. Han, H. Yu, T. Yang, S. Wang, X. Wang, Magnetic activated-ATP@Fe3O4 nanocomposite as an efficient Fenton-like heterogeneous catalyst for degradation of ethidium bromide, *Sci. Rep.* 7 (2017) 6070, <https://doi.org/10.1038/s41598-017-06398-3>.
 - [18] Y. Matsumoto, N. Terui, S. Tanaka, Electrochemical Detection and Control of Interactions between DNA and Electroactive Intercalator Using a DNA–Alginate Complex Film Modified Electrode, *Environ. Sci. Technol.* 40 (2006) 4240–4244, <https://doi.org/10.1021/es060084x>.
 - [19] Y. Matsumoto, N. Terui, S. Tanaka, Accumulated detection of ethidium bromide using a UV-irradiated DNA film modified electrode and its application for electrochemical detection of an environmental pollutant, *J. Electroanal. Chem.* 610 (2007) 193–198, <https://doi.org/10.1016/j.jelechem.2007.07.010>.
 - [20] H.N. Cheng, L.J. Doemeny, C.L. Geraci, D. Grob Schmidt, Nanotechnology Overview: Opportunities and Challenges, in: H.N. Cheng, L. Doemeny, C.L. Geraci, D. Grob Schmidt (Eds.), ACS Symposium Series, American Chemical Society, Washington, DC, 2016, pp. 1–12, <https://doi.org/10.1021/bk-2016-1220.ch001>.
 - [21] L.H. Hoang, P.V. Hanh, N.D. Phu, X.-B. Chen, W.C. Chou, Synthesis and characterization of MnWO4 nanoparticles encapsulated in mesoporous silica SBA-15 by fast microwave-assisted method, *J. Phys. Chem. Solids* 77 (2015) 122–125, <https://doi.org/10.1016/j.jpcs.2014.10.013>.
 - [22] Z. Jiang, F. Zhang, L. Shen, T. Ge, Y. Zhang, Facile pH-controlled synthesis of MnWO4 nanoparticles and nanorods and their heterogeneous Fenton-like catalytic activity, *Mater. Lett.* 293 (2021), 129662, <https://doi.org/10.1016/j.matlet.2021.129662>.
 - [23] H. Zhou, J. Ke, D. Xu, J. Liu, MnWO4 nanorods embedded into amorphous MoSx microsheets in 2D/1D MoSx/MnWO4 S-scheme heterojunction for visible-light photocatalytic water oxidation, *J. Mater. Sci. Technol.* 136 (2023) 169–179, <https://doi.org/10.1016/j.jmst.2022.07.021>.
 - [24] S. Saranya, S.T. Senthilkumar, K.V. Sankar, R.K. Selvan, Synthesis of MnWO4 nanorods and its electrical and electrochemical properties, *J. Electroceram* 28 (2012) 220–225, <https://doi.org/10.1007/s10832-012-9714-7>.
 - [25] M. Mai, C. Feldmann, Microemulsion-based synthesis and luminescence of nanoparticulate CaWO4, ZnWO4, CaWO4:Tb, and CaWO4:Eu, *J. Mater. Sci.* 47 (2012) 1427–1435, <https://doi.org/10.1007/s10853-011-5923-8>.
 - [26] A. Tiwari, V. Singh, T.C. Nagaiath, Tuning the MnWO4 morphology and its electrocatalytic activity towards oxygen reduction reaction, *J. Mater. Chem. A* 6 (2018) 2681–2692, <https://doi.org/10.1039/C7TA10380H>.
 - [27] W. Wang, N. Wu, J.-M. Zhou, F. Li, Y. Wei, T.-H. Li, X.-L. Wu, MnWO4 nanoparticles as advanced anodes for lithium-ion batteries: F-doped enhanced lithiation/delithiation reversibility and Li-storage properties, *Nanoscale* 10 (2018) 6832–6836, <https://doi.org/10.1039/C7NR08716K>.
 - [28] V. Rathi, A. Pannierselvar, R. Sathiyapriya, Surface decoration of MnWO4 nanoparticles with g-C3N4 nanosheets to build hetero-structure and its structural, optical and enhanced visible light photocatalytic activity, *J. Mater. Sci. Mater.*

- [44] M. Athar, M. Fiaz, M.A. Farid, M. Tahir, M.A. Asghar, S. ul Hassan, M. Hasan, Iron and Manganese Codoped Cobalt Tungstates $\text{Co}_{1-(x+y)}\text{Fe}_x\text{Mn}_y\text{WO}_4$ as Efficient Photoelectrocatalysts for Oxygen Evolution Reaction, *ACS Omega* 6 (2021) 7334–7341, <https://doi.org/10.1021/acsomega.0c05412>.
- [45] C.-C. Ting, W.-Y. Li, C.-H. Wang, H.-E. Yong, Structural and electrical properties of the europium-doped indium zinc oxide thin film transistors, *Thin Solid Films* 562 (2014) 625–631, <https://doi.org/10.1016/j.tsf.2014.04.052>.
- [46] Frontiers | Europium-Doped Ceria Nanowires as Anode for Solid Oxide Fuel Cells, (n.d.). (<https://www.frontiersin.org/articles/10.3389/fchem.2020.00348/full>) (accessed September 24, 2022).
- [47] U. Gattermann, G. Benka, A. Bauer, A. Senyshyn, S.-H. Park, Magnetic properties of the In-doped MnWO_4 -type solid solutions $\text{Mn}_{1-3x}\text{In}_{2x}\square_x\text{WO}_4$ [\square =vacancy; $0 \leq x \leq 0.11$], *J. Magn. Mater.* 398 (2016) 167–173, <https://doi.org/10.1016/j.jmmm.2015.09.033>.
- [48] U. Gattermann, S.-H. Park, M. Kaliwoda, Synthesis and characterisation of In-doped MnWO_4 -type solid-solutions: $\text{Mn}_{1-3x}\text{In}_{2x}\square_x\text{WO}_4$ ($x=0-0.11$), *J. Solid State Chem.* 219 (2014) 191–200, <https://doi.org/10.1016/j.jssc.2014.07.039>.
- [49] J.R. Günter, H.W. Schmalle, E. Dubler, Crystal structure and properties of a new magnesium heteropoly-tungstate, $\text{Mg}_7(\text{MgW}_{12}\text{O}_{42})(\text{OH})_4(\text{H}_2\text{O})_8$, and the isostructural compounds of manganese, iron, cobalt and nickel, *Solid State Ion.* 43 (1990) 85–92, [https://doi.org/10.1016/0167-2738\(90\)90474-6](https://doi.org/10.1016/0167-2738(90)90474-6).
- [50] A. Marković, S. Savić, A. Kukuruzar, Z. Konya, D. Manojlović, M. Ognjanović, D. M. Stanković, Differently Prepared PbO_2 /Graphitic Carbon Nitride Composites for Efficient Electrochemical Removal of Reactive Black 5 Dye, *Catalysts* 13 (2023) 328, <https://doi.org/10.3390/catal13020328>.
- [51] R.M. Belal, M.A. Zayed, R.M. El-Sherif, N.A. Abdel Ghany, Advanced electrochemical degradation of basic yellow 28 textile dye using IrO_2/Ti meshed electrode in different supporting electrolytes, *J. Electroanal. Chem.* 882 (2021), 114979, <https://doi.org/10.1016/j.jelechem.2021.114979>.
- [52] The ORCA program system - Neese - 2012 - WIREs Computational Molecular Science - Wiley Online Library, (n.d.). (<https://wires.onlinelibrary.wiley.com/doi/full/10.1002/wcms.81>) (accessed November 30, 2022).
- [53] R.S. Mulliken, Electronic Population Analysis on LCAO-MO Molecular Wave Functions. IV. Bonding and Antibonding in LCAO and Valence-Bond Theories, *J. Chem. Phys.* 23 (2004) 2343, <https://doi.org/10.1063/1.1741877>.
- [54] R.S. Mulliken, Electronic Population Analysis on LCAO-MO Molecular Wave Functions. II. Overlap Populations, Bond Orders, and Covalent Bond Energies, *J. Chem. Phys.* 23 (2004) 1841, <https://doi.org/10.1063/1.1740589>.
- [55] I. Zimmermann, H. Zimmermann, pKa-Werte von Ethidiumbromid und 7-Amino-9-phenyl-10-äthyl-phenanthridinium-bromid / pKa-Values of Ethidiumbromide and 7-Amino-9-phenyl-10-ethyl-phenanthridinium-bromide, *Z. Für Naturforsch. C.* 31 (1976) 656–660, <https://doi.org/10.1515/znc-1976-11-1205>.
- [56] N.W. Luedtke, Q. Liu, Y. Tor, On the Electronic Structure of Ethidium, *Chem. – A Eur. J.* 11 (2005) 495–508, <https://doi.org/10.1002/chem.200400559>.
- [57] J. Loccufier, E. Schacht, Regioselective acylation of 3,8-diamino-5-ethyl-6-phenyl-phenanthridinium bromide, preparation of potential new trypanocides, *Tetrahedron* 45 (1989) 3385–3396, [https://doi.org/10.1016/S0040-4020\(01\)81017-6](https://doi.org/10.1016/S0040-4020(01)81017-6).
- [58] D. Reha, M. Kabeláč, F. Ryjáček, J. Šponer, J.E. Šponer, M. Elstner, S. Suhai, P. Hobza, Intercalators. 1. Nature of Stacking Interactions between Intercalators (Ethidium, Daunomycin, Ellipticine, and 4',6-Diaminide-2-phenylindole) and DNA Base Pairs. Ab Initio Quantum Chemical, Density Functional Theory, and Empirical Potential Study, *J. Am. Chem. Soc.* 124 (2002) 3366–3376, <https://doi.org/10.1021/ja011490d>.
- [59] P.U. Giacomoni, M. Le Bret, Electronic structure of ethidium bromide, *FEBS Lett.* 29 (1973) 227–230, [https://doi.org/10.1016/0014-5793\(73\)80025-0](https://doi.org/10.1016/0014-5793(73)80025-0).
- [60] G. Thomas, B. Roques, Proton magnetic resonance studies of ethidium bromide and its sodium borohydride reduced derivative, *FEBS Lett.* 26 (1972) 169–175, [https://doi.org/10.1016/0014-5793\(72\)80566-0](https://doi.org/10.1016/0014-5793(72)80566-0).
- [61] R.W. Layer, The chemistry of imines, *Chem. Rev.* 63 (1963) 489–510, <https://doi.org/10.1021/cr60225a003>.
- [62] A.C. Dash, B. Dash, S. Praharaj, Hydrolysis of imines: kinetics and mechanism of spontaneous acid-, base-, and metal ion-induced hydrolysis of N-salicylidene-2-aminothiazole, *J. Chem. Soc., Dalton Trans.* (1981) 2063–2069, <https://doi.org/10.1039/DT9810002063>.
- [63] J. Hine, J.C.J.R. Craig, J.G.I. Underwood, F.A. Via, Kinetics and mechanism of the hydrolysis of N-isobutylidenemethylamine in aqueous solution, *J. Am. Chem. Soc.* 92 (1970) 5194–5199, <https://doi.org/10.1021/ja00720a032>.